Channel Prediction and Adaptation over Satellite Channels with Weather-Induced Impairments

by

Jihwan Patrick Choi

B.S. Electrical Engineering
Seoul National University (1998)

Submitted to the Department of Electrical Engineering and Computer Science
in partial fulfillment of the requirements for the degree of

Master of Science
in
Electrical Engineering and Computer Science
at the

Massachusetts Institute of Technology

May 2000

Author .....
Department of Electrical Engineering and Computer Science
May 19, 2000

Certified by .....
Vincent W. S. Chan
Professor of Electrical Engineering and Computer Science
Thesis Supervisor

Certified by .....
Arthur C. Smith
Chairman, Department Committee on Graduate Students

Channel Prediction and Adaptation over Satellite Channels with Weather-Induced Impairments

by

Jihwan Patrick Choi

Submitted to the Department of Electrical Engineering and Computer Science
on May 5, 2000, in partial fulfillment of the requirements for the degree of
Master of Science in Electrical Engineering and Computer Science

Abstract

Bad weather conditions, especially due to rain, cause satellites operating at high frequencies (above 10 GHz) to have significant link attenuation. Usually extra link margins are used to assure link availability. These margins cause inefficient use of precious satellite and terminal power, and unnecessarily limit data throughputs. Efficiency improvements using channel prediction and adaptation over satellite channels with weather-induced impairments are considered in this thesis.

First, we consider scintillation and rain attenuation as two dominant factors for signal fading over satellite-earth paths above 10 GHz, and explore physical and mathematical modeling of the two processes. Statistical and spectral analyses of these processes using one or two pole autoregressive (AR) models yield simple linear estimators for the received signal attenuation. Using these estimators, we present results where we can predict the received signal attenuation within ± 0.5 dB 1 second ahead and within ± 1.0 dB 4 seconds ahead.

For adaptation, we change the signal transmission power, the modulation symbol size, and the code rate adaptively. In particular, we suggest a *continuous power control and discrete rate control* strategy, through which we build a set of modulation/code states, and discretely change the modulation symbol size and the code rate from state to state. Within each state, continuous power control is implemented. Several examples that use this technique and quantitative analyses of power increase and capacity are provided. The analyses indicate that there is a substantial gain in performance either in capacity and/or power consumption with the adaptive schemes.

Thesis Supervisor: Vincent W. S. Chan
Title: Joan and Irwin Jacobs Professor of Electrical Engineering
and Computer Science; and Aeronautics and Astronautics
Director, Laboratory for Information and Decision Systems

Acknowledgments

I would like to express my deep gratitude to my advisor, Professor Vincent Chan, for his warm encouragement and guidance. He has not only led a beginning researcher, named Jihwan, into the first entrance to the world of research, but also helped a newcomer, also named Jihwan, easily adjust himself to the New World, MIT.

I am grateful to DARPA for making my master's research possible. I also thank KFAS for their support for my study here at MIT.

My parents have always devoted themselves to their only child. Their deep love and solid trust have made me who I am. Last, but not least, I would like to give my deep thanks to them, *my Father and Mother.*

Table of Contents

List of Figures

List of Tables

Chapter 1

Introduction

1.1 Motivation and Scope

So far, the primary applications of satellite communications have been TV broadcasting, telephony trunking, military communications, and data relay for space missions. Satellites can provide services to mobile users as well as fixed ground users while the terrestrial networks (fiber and wireless) can only cover terrestrial users on the ground where there are fiber and wireless infrastructures leaving coverage gaps in the populated areas, over the ocean, and in the air. In recent years, many schemes to utilize satellites not only for mobile telephone service but also for data communications have been suggested. To varying extents, all the schemes include building a heterogeneous network, which interconnects the satellites among themselves and with the terrestrial wired/wireless networks.

As the needs for high data rate in satellite communications increase, the frequencies used are going up since lower frequency bands are already crowded. Many satellite communication systems such as Teledesic will use the high-frequency Ka-band (20/30 GHz). The drawback of this high-frequency band is that it is vulnerable to signal attenuation due to bad weather, especially rain. Thus, to provide reliable communications during rainy periods, current satellite systems usually provide an extra power margin over the power requirements for good weather conditions. However, this margin, which is sized to pro-

vide enough link power in bad weather conditions, is significant at high-frequencies (about 10 ~ 20 dB at 20/30 GHz). If the system were made to provide this relatively high power margin all the time, regardless of weather conditions, it would represent a very inefficient use of power, which is one of the most precious resources of satellite systems.

Fully adaptive schemes that vary the modulation symbol size, the code rate, the transmitter power of the signal, or all of these together, according to weather conditions, will improve efficiency tremendously. In order to implement these adaptive schemes, first we need to sense the current state of the time-varying satellite channels that are induced by changing weather conditions. For this work, we will treat the received signal attenuation due to weather conditions as a random process. We will characterize this process with the aid of data, and create an appropriate stochastic model. Using this model and various link monitoring techniques, we can then predict the future channel state and the corresponding time-varying channel capacity based on the link monitoring information. With channel observation and prediction combined, we will explore the possibilities of dynamically adapting the transmission power, the modulation symbol size and the code rates, and quantify potential performance improvements in this thesis.

1.2 Outline of this Thesis

The main focus of this work is to characterize high-frequency satellite channels with weather-induced impairments, and develop channel prediction and adaptation schemes for very efficient and reliable communication systems.

This thesis consists of three main chapters:

channel modeling and prediction

channel adaptation

conclusions and future research

The contents that will be presented in each chapter are as follows.

Chapter 2:

In this chapter, we will address channel modeling and prediction. First, we will consider rain attenuation and scintillation of the received signal as two main causes of the signal fading process over the satellite-earth channels at high frequencies such as Ka-band, and explore physical and mathematical characteristics of the signal attenuation process due to rain attenuation and scintillation. Then, spectral analysis of the attenuated signals using autoregressive (AR) models will be discussed. Based on a stochastic model developed, we will establish a real-time prediction method for future signal attenuation. Finally, we provide some examples where we apply our prediction scheme.

Chapter 3:

In this chapter, we will present a channel adaptation issue based on channel models and prediction methods discussed in Chapter 2. In particular, we will suggest a continuous power control and discrete rate control strategy. We will first review the general methodologies used for power and rate control in satellite communications, and describe how our continuous power control and discrete rate control scheme works. Some examples using the adaptive scheme and quantitative analyses of power increase and capacity will be provided. This chapter will conclude that there is substantial

improvement on the average rate and/or the power consumption with the adaptive scheme.

Chapter 4:

Finally, we will present conclusions and future research directions.

Chapter 2

Channel Modeling and Prediction

2.1 Introduction

In satellite-earth communications at high frequencies (above 10 GHz), the earth-space atmospheric channels exhibit fading behavior, and this fading causes deterioration of the channel and increases the bit error rate (BER). To mitigate these degenerating effects, we must either vary the data rate or improve the channel. Doing this adaptively with high efficiency (in terms of utility of satellite and terrestrial resources) is the ultimate goal of this thesis. To implement a channel adaptation scheme for communication systems, we need to study the characteristics of the channel, develop an appropriate mathematical model of the channel, and use this model to predict channel variations a few seconds ahead within a small range of tolerable errors.

In Section 2.2, we will see that this fading process mainly comes from rain attenuation and scintillation of the received signal [1, 2]. We will model these two main effects as random processes that are lognormally distributed. In Section 2.3 and 2.4, with statistical and spectral analysis of rain attenuation and scintillation data, we will introduce a stochastic

model and utilize this model to make real-time predictions of the received signal attenuation.

2.2 Signal Attenuation due to Scintillation and Rain

Signal attenuation through satellite-earth paths substantially contributes to the characteristics of the time-varying fading satellite channels. Among many factors, signal attenuation due to rain along satellite-earth paths at high frequencies (above 10 GHz) is the predominant signal impairing factor. However, scintillation effects cannot be ignored in the case of good weather conditions when there is no rain attenuation. In addition, scintillation must be taken into account for low power margin system designs. Therefore, though there are also other contributions such as the absorption by moisture in the air, it is known that rain attenuation and amplitude scintillation dominate the Ka-band fading process [1, 2]. In this section, we explore the physical and mathematical interpretation of these two processes: received signal scintillation and rain attenuation.

2.2.1 Scintillation

Scintillation refers to the rapid fluctuations of the amplitude and the phase at the receiver, as a result of phase front distortions by small-scale refractive index irregularities in the path with time. The phase front planes that are originally parallel near the source on satellite-earth paths are distorted when they pass through the small scale irregularities of the

refractive index caused by turbulence in the air. This can result in constructive or destructive interference of the signal intensity at the receiving plane according to the phase differences through different paths. In addition, if multiple receivers are used, phase front fluctuations at the receiving plane can yield fluctuations in the angle of arrival and signal power.

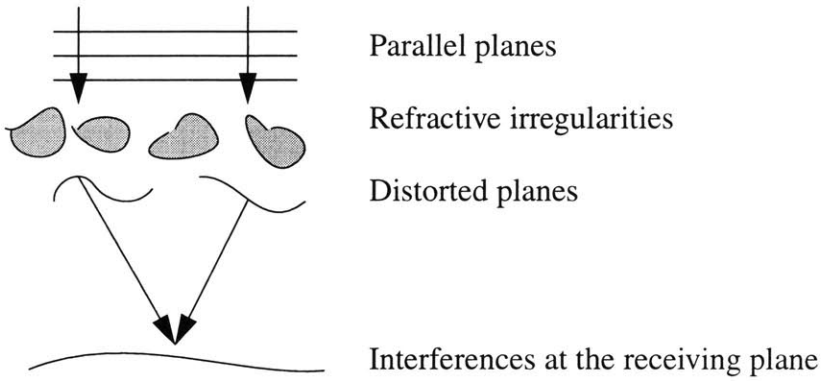

Figure 2.1: Scintillation Process in the Atmosphere

Fig. 2.2 shows the typical behavior of the time dynamics of the received intensity scintillation process. The data have been measured at 19.5 GHz on satellite-earth paths during 100 seconds on two different clear days and show amplitude fluctuations of ± 1 dB or so. Most fluctuations last about one or two seconds. Though longer term effects such as absorption by gas and moisture in the air had been included in the raw data, they have been removed to show the characteristics of the fluctuations alone in Fig. 2.2.

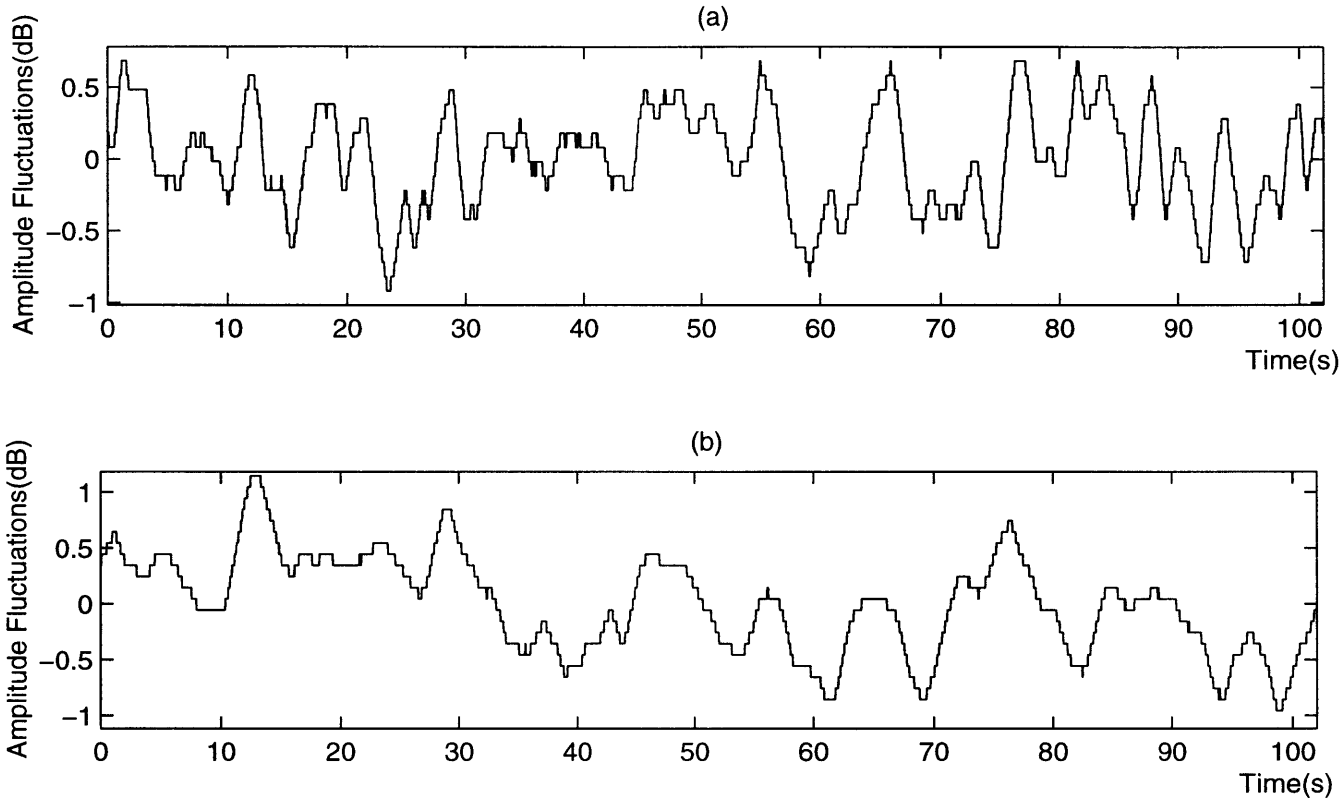

Figure 2.2: Typical Examples of a Scintillation Process

The amplitude scintillation process has been modeled by Moulsley and Vilar [3]. The log amplitude of scintillation has a zero-mean conditionally normal distribution (i.e., the amplitude is lognormal in a linear scale.) with the variance of scintillation σ^2, lognormally distributed by itself. If we denote the amplitude scintillation as a random process $e(t)$ and define $z(t) \equiv \ln e(t)$, the probability density function (PDF) of $z(t)$ in the Moulsley-Vilar model is given as:

$$p_Z(z) = \int p_{Z,\sigma^2}(z, \sigma^2) d\sigma^2$$

$$= \int p_{Z|\sigma^2}(z|\sigma^2) \cdot p_{\sigma^2}(\sigma^2) d\sigma^2$$

$$= \int \frac{1}{\sqrt{2\pi\sigma^2}} \cdot \exp\left[-\frac{z^2}{2\sigma^2}\right] \cdot \frac{1}{\sigma^2\sigma_\sigma\sqrt{2\pi}} \cdot \exp\left[-\frac{(\ln\sigma^2 - \ln\sigma_m^2)^2}{2\sigma_\sigma^2}\right] d\sigma^2, \tag{2.1}$$

where $\ln\sigma_m^2$ and σ_σ^2 are the mean and the variance of $\ln\sigma^2$ respectively.

For short durations (up to 1 minute), the variance can be considered as a constant; i.e., the short-term distribution of the log amplitude $z(t)$ of scintillation may be considered normal with a constant variance σ^2 with the following PDF:

$$p_Z(z) = \frac{1}{\sigma\sqrt{2\pi}} \cdot \exp\left(-\frac{z^2}{2\sigma^2}\right), \tag{2.2}$$

where $z(t) \equiv \ln e(t)$ and $-\infty < z(t) < \infty$.

This can be verified in the following normalized distributions of time-series data of the scintillation. The PDFs of lognormal distributions with the corresponding variance have been also plotted for comparison. The data shows excellent agreement.

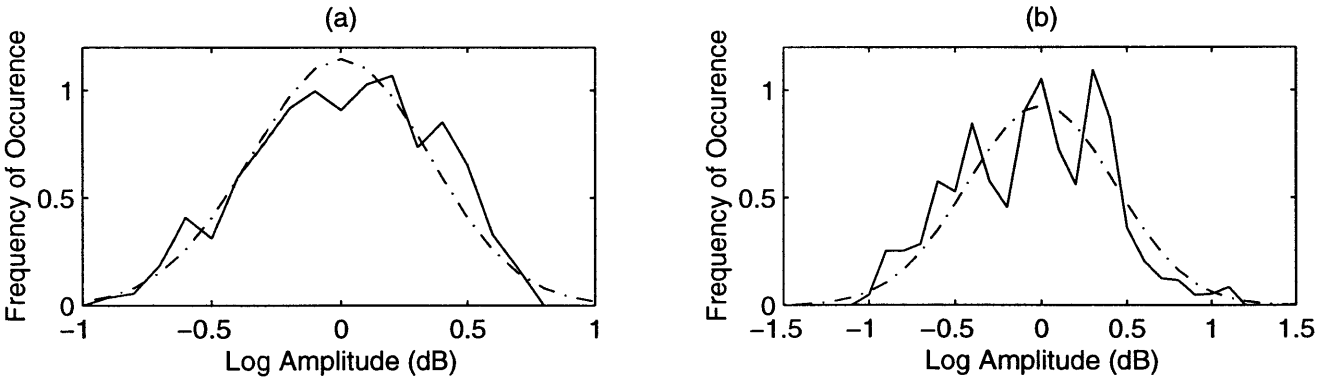

Figure 2.3: Normalized Distributions (solid) of Log Amplitudes of Scintillation Attenuated Signals in Fig. 2.2 and Corresponding Lognormal Distributions (dotted)

2.2.2 Rain Attenuation

Rain attenuation dominates the fading process at high frequencies, for example, Ka-band, in satellite-earth communications. The amplitude attenuation due to rain can be as high as

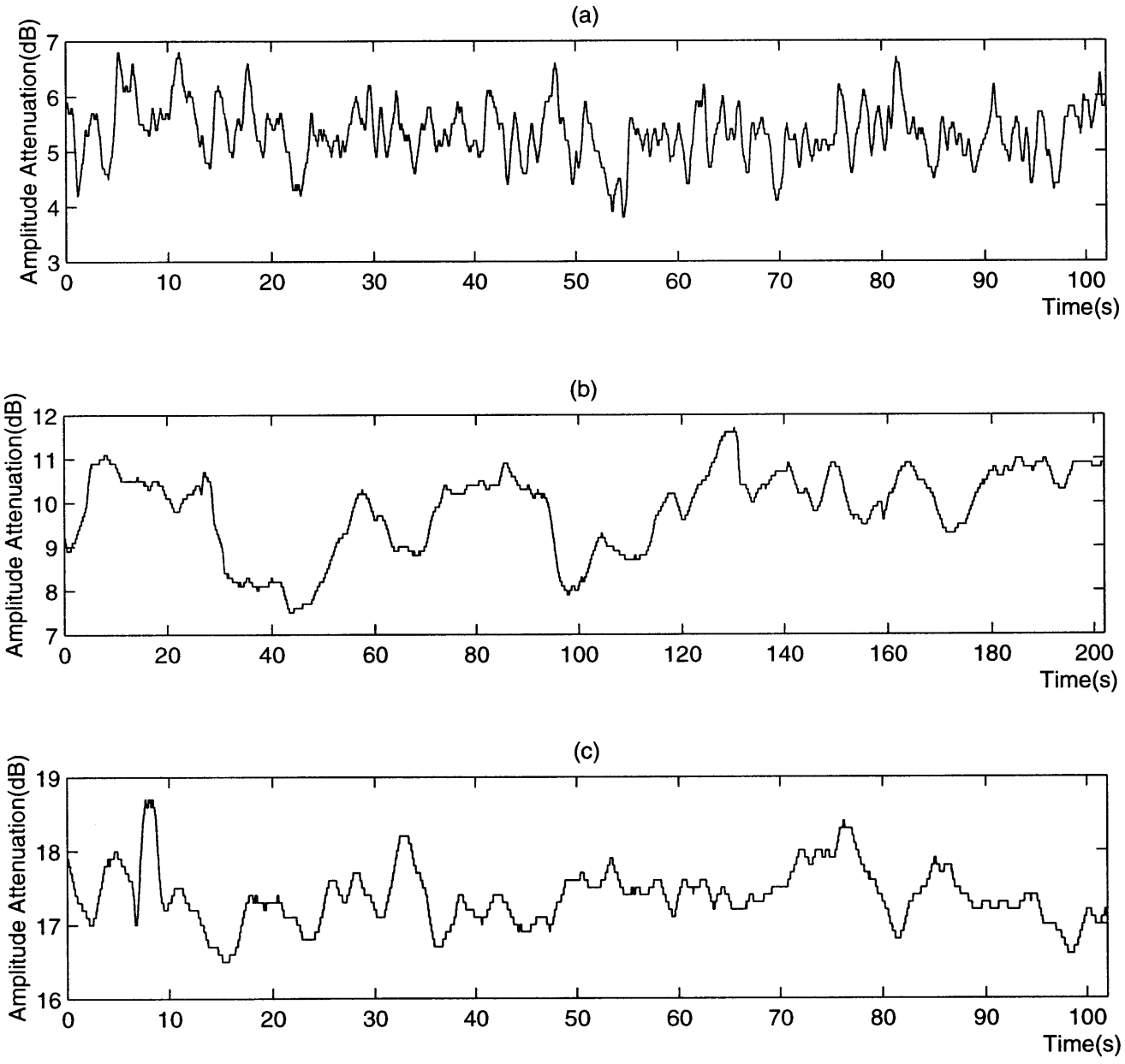

Figure 2.4: Typical Examples of Rain Attenuation Process; (a) for Light Rain (b) for Moderate Rain (c) for (Moderately) Heavy Rain

20 dB (with rare occurrences up to 40 dB). Fig. 2.4 shows three typical time-series of rain attenuated signals, which have been measured at 19.5 GHz on satellite-earth paths in a variety of rain rate conditions.

The rain attenuation of the signal can be modeled as a random process $x(t)$, whose log amplitude $y(t) \equiv \ln x(t)$ is also shown to be normally distributed[1] with the following PDF:

$$p_Y(y) = \frac{1}{\sigma\sqrt{2\pi}} \cdot \exp\left(-\frac{(y-m)^2}{2\sigma^2}\right), \tag{2.3}$$

where $-\infty < y(t) < \infty$.[2]

We can also see the lognormality of rain attenuation in the following histograms of time-series data of rain attenuated signals with the corresponding lognormal PDFs in Fig. 2.5. In the case of (b), we can see that the histogram does not agree with the lognormal distribution as well since the coherence time of this process is long compared to the sampling period, and our total data length (200 seconds) is not long enough to get independent looks. In Fig. 2.4 (b), we can see that the period of fluctuations of process (b) is longer than those of (a) and (c).

---

1. This can be understood as the result of the central limit theorem (CLT) [4]. Let us assume the amplitude of the received signal to be $x(t)$. We can model $x(t)$ as a result of a sequence of small attenuations $\{a_i\}$ cascaded in series, and the $\{a_i\}$'s are independent identically distributed (i.i.d) random variables. Thus, if the transmitted signal is $s(t)$, $x(t) = \prod_i a_i s(t)$ and $\ln x(t) = \sum_i \ln a_i + \ln s(t)$. Then, $\ln x$ converges to a Gaussian random variable by the CLT since $\{\ln a_i\}$'s are also i.i.d. and has a bounded variance. Therefore, the distribution of amplitude attenuation of the signal approaches the lognormal distribution.

2. The log amplitudes of rain attenuation cannot be negative, strictly speaking. However, we assume that the range of log amplitude is from $-\infty$ to ∞ for easy calculation of its moments. Moreover, when we combine the scintillation effects with the rain attenuation process, it makes more sense to define the range of the log amplitude of signal attenuation to be from $-\infty$ to ∞ throughout this thesis, to include the constructive interference effects of the scintillation process even though we use the term 'attenuation.'

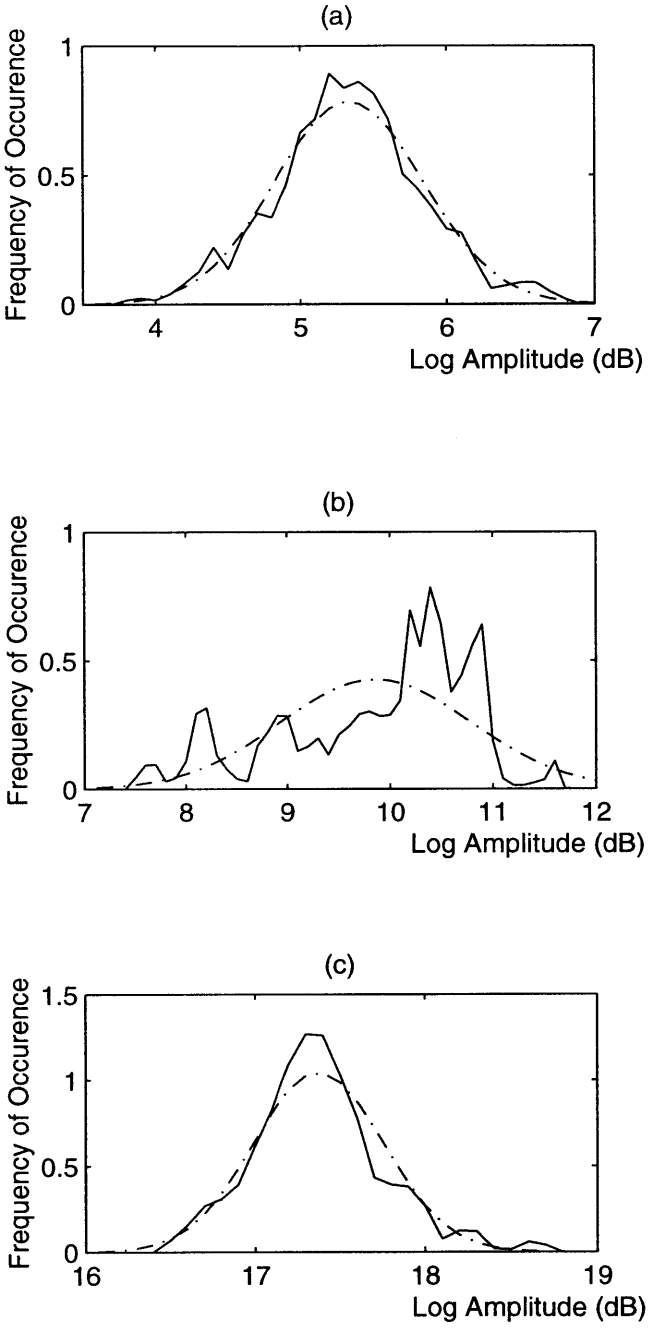

Figure 2.5: Normalized Distributions (solid) of Rain Attenuated Signals in Fig. 2.4 and Corresponding Lognormal Distributions (dotted); (a) for Light Rain (b) for Moderate Rain (c) for (Moderately) Heavy Rain

2.3 Spectral Analysis of Attenuated Signals

In order to arrive at a prediction model for the signal attenuation, where the future path attenuation is predicted based on a short segment of past measured data, first we need to analyze the spectral characteristics of the received signal attenuation due to rain and scintillation.

Fig. 2.6 shows two sampled power spectral densities (PSDs) of the received signal attenuation in different weather conditions. The sampled PSDs have been obtained by using averaged periodograms. The autoregressive (AR) models in solid lines have been derived from the data using the standard techniques described in Appendix A.

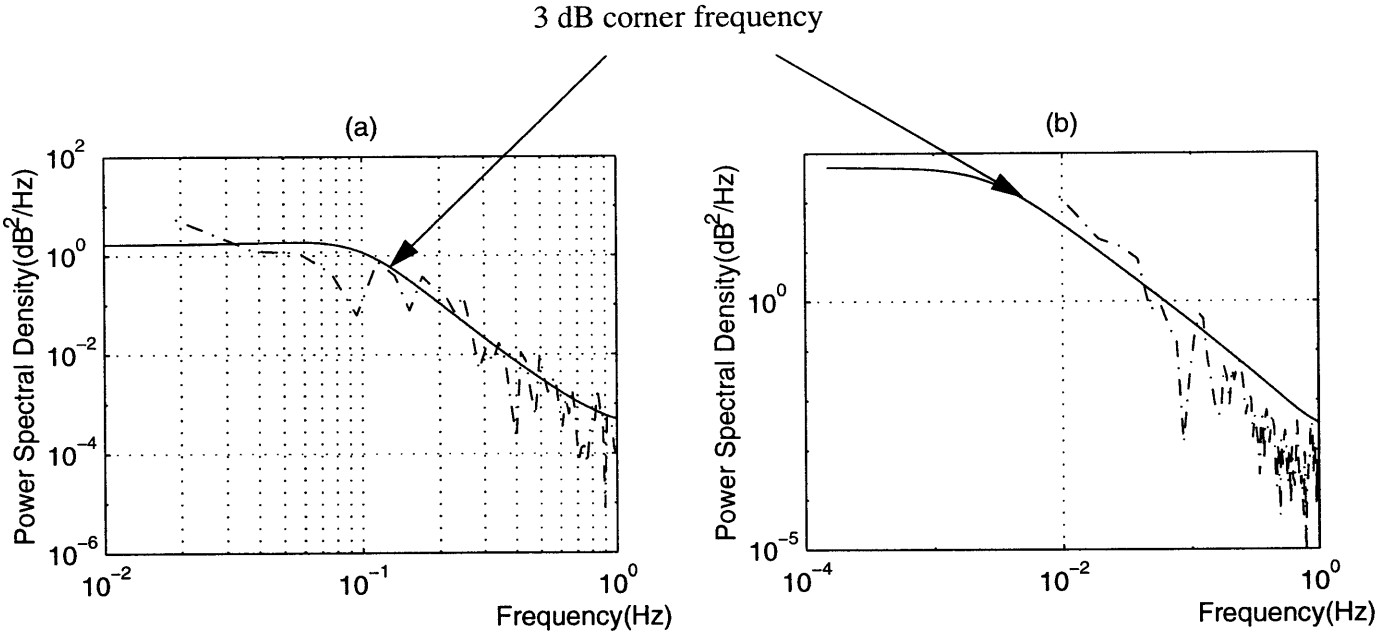

Figure 2.6: Sampled PSDs using Averaged Periodograms (dotted) and Corresponding AR Models (solid) (a) on a Clear Day (b) on a Moderately Rainy Day

In AR models, the signal attenuation over satellite-earth channels is modeled as the output of an all-pole filter, $H(z)$, driven by zero-mean white noise. Using the techniques described in Appendix A, we have obtained the all-pole filter models shown in Fig. 2.6 as follows:

$$\text{(a) } H(z) = \frac{1}{1 - 1.6904z^{-1} + 0.7447z^{-2}}$$

$$\text{(b) } H(z) = \frac{1}{1 - 1.1726z^{-1} + 0.1784z^{-2}}.$$

We believe the attenuation on a clear day mainly comes from the scintillation effects alone, and the attenuation on a moderately rainy day comes mostly from rain attenuation with negligible scintillation effects.

From our analysis represented in Fig 2.6 and the literature [5, 6, 7, 8], we can see that scintillation and rain attenuation processes have time-invariant spectral characteristics for short durations. For scintillation, the scintillation frequency or the fading rate is below 1 Hz, with a corner frequency of about 0.1 Hz, and its power spectrum generally rolls off faster than -20 dB/decade. [5] shows that the scintillation process has a PSD with a slope range of -23 ~ -37 dB/decade. On the other hand, the power spectrum of rain attenuation has a slope of -20 dB/decade and a corner frequency of the order of 10^{-3} ~ 10^{-4} Hz [6, 7, 8][1].

Here, we focus on the slopes of the PSDs, which not only give the number of poles in the AR models but suggest the number of past data samples used in our prediction model, which we will explore further in the next section. In our analysis and the literature, the rain attenuation has a slope of f^{-2}, while the scintillation has that of $f^{-2.3}$ ~ $f^{-3.7}$.

1. [6], [7], [8], and our analysis in Fig. 2.6 show that the corner frequencies are 1.85×10^{-3} Hz, 2.33×10^{-3} Hz, 1.63×10^{-4} Hz, and 3.0×10^{-3} Hz respectively.

Therefore, we can conclude that one pole AR models[1] can describe the rain attenuation process, while one or two pole AR models can describe the scintillation.

2.4 Real-Time Channel Prediction

Now we move to the stage where we make a prediction model of future signal attenuation based on the past. In the section above, we observed that the scintillation process can be expressed by an AR model with one or two poles, while the rain attenuation process can be expressed with one pole only. We use these AR models in our prediction models.

We consider the signal attenuation by weather conditions on satellite-earth paths as a stochastic process. Furthermore, we have seen that signal fluctuations can be well modeled using an AR model, where the signal attenuation $y[n]$ is modeled as the output of an all - pole filter driven by a zero-mean white noise process $w[n]$, so that we can get the expression $y[n] = \sum_{i=1}^{M} a_i y[n-i] + w[n]$, where M is the order of the AR process.

Our problem is to determine the b_i's in the linear prediction equation

$$\hat{y}[n] = \sum_{i=1}^{\infty} b_i y[n-i]. \tag{2.4}$$

We can solve this problem using the following lemma.

1. Of course, a more-than-one pole AR model can describe the rain attenuation process better as in Fig. 2.6 (b), where a two pole AR model has been used. However, a one pole AR model gives sufficient description with the smaller number of past data, which has the advantages of memory saving and fast implementation.

Lemma:

If a random process that is zero-mean wide-sense stationary (WSS) is known to be an AR process,

$$y[n] = \sum_{i=1}^{M} a_i y[n-i] + w[n], \tag{2.5}$$

where $w[n]$ is a zero-mean additive white Gaussian noise (AWGN) process, then the linear least-squares (LLS) estimator (Appendix B) is

$$\hat{y}[n] = \sum_{i=1}^{M} a_i y[n-i]. \tag{2.6}$$

Proof:

Let $\hat{y}[n]$ be

$$\hat{y}[n] = \sum_{i=1}^{\infty} b_i y[n-i]. \tag{2.7}$$

By the orthogonality principle (Appendix B) of LLS estimation, the optimal predictor has the property that the corresponding errors are orthogonal to the data,

$$\begin{aligned} & E[(\hat{y}[n] - y[n])y[n-k]] \\ &= E\left[\left(\sum_{i=1}^{M}(b_i - a_i)y[n-i] + \sum_{j=M+1}^{\infty} b_j y[n-j]\right)y[n-k] - w[n]y[n-k]\right] \\ &= E\left[\left(\sum_{i=1}^{M}(b_i - a_i)y[n-i] + \sum_{j=M+1}^{\infty} b_j y[n-j]\right)y[n-k]\right] \quad \text{for } k = 1, 2, \ldots, M \\ &= 0, \end{aligned} \tag{2.8}$$

where the second equality follows from the fact that $w[n]$ is independent of $y[n-k]$ and has a zero mean. Thus,

$$\begin{aligned} b_i &= a_i \qquad 1 \le i \le M \\ &0 \qquad i > M \end{aligned} \tag{2.9}$$

is a trivial solution of (2.8). Therefore, $\hat{y}[n] = \sum_{i=1}^{M} a_i y[n-i]$ is the LLS estimator of $y[n]$. Moreover, since $y[i]$'s are jointly Gaussian, the LLS estimator (2.6) becomes the optimal minimum mean-square error (MMSE) estimator (Appendix B) in this case.

■

Therefore, in our case, the prediction equation is

$$\hat{y}[n] = a_1 y[n-1] \qquad \text{or} \tag{2.10}$$

$$\hat{y}[n] = a_1 y[n-1] + a_2 y[n-2] \tag{2.11}$$

according to whether the AR process is of order of one or two.

In general, at time n, we want to predict the future further, i.e., $\hat{y}[n+1]$, $\hat{y}[n+2]$,..., $\hat{y}[n+j]$ based on $y[n-1]$, $y[n-2]$,..., $y[n-k]$. Since we are using the AR model with one or two poles, we restrict the number of the past data used in prediction to that of poles in our AR models, i.e., one or two. Then our general prediction equation is

$$\hat{y}[n+j] = c_1 y[n-1] \qquad \text{or} \tag{2.12}$$

$$\hat{y}[n+j] = c_1 y[n-1] + c_2 y[n-2], \tag{2.13}$$

where $j \ge 0$ determines how far ahead the predictor will tell the future.

In order to obtain the prediction coefficient c_i's, we use the modified *Yule-Walker* equation [9]. From the orthogonality principle again, in the two-pole case,

$$E[(\hat{y}[n+j]-y[n+j])\cdot y[n-k]] = 0 \qquad \text{for } k = 1, 2, \tag{2.14}$$

which can be written in the form of

$$E\left[\sum_{l=1}^{2} c_l \cdot y[n-l]\cdot y[n-k]\right] = E[y[n+j]\cdot y[n-k]] \qquad \text{for } k = 1, 2. \tag{2.15}$$

Hence, using the covariance function of $y[n]$, $K_{yy}[m] = E[y[n]y[n+m]]$,

$$\sum_{l=1}^{2} c_l K_{yy}[k-l] = K_{yy}[k+j] \qquad \text{for } k = 1, 2, \tag{2.16}$$

which is, in a matrix form,

$$\begin{bmatrix} K_{yy}[0] & K_{yy}[1] \\ K_{yy}[1] & K_{yy}[0] \end{bmatrix} \begin{bmatrix} c_1 \\ c_2 \end{bmatrix} = \begin{bmatrix} K_{yy}[1+j] \\ K_{yy}[2+j] \end{bmatrix}. \tag{2.17}$$

The c_i's are obtained by solving the matrix equation, (2.17). (2.12) and (2.13) with c_i's obtained in (2.17) satisfy (2.14), in the same way as in the case of $j = 0$ in the lemma. Therefore, (2.12) and (2.13) are the LLS estimators, and moreover, the MMSE estimators in this case of AWGN.

Since we do not know the exact characteristic of $y[n]$, which implies that we do not know the exact value of $K_{yy}[m]$, we first must also estimate $K_{yy}[m]$ itself. One simple way to obtain an estimate of $K_{yy}[m]$, $\hat{K}_{yy}[m]$ is to use the sample correlation function from some number of the past data. We will use N past values of $y[n]$ for the calculation of $\hat{K}_{yy}[m]$,

$$\hat{K}_{yy}[m] = \frac{1}{N-|m|} \sum_{k=0}^{N-1-|m|} y[k]y[k+|m|] \qquad |m| \le N-1 \tag{2.18}$$

$$0 \qquad \text{otherwise.}$$

The number N of the past data used in the sample correlation function depends on the coherence time τ of the process that we deal with. When $N \sim \tau$, we expect an accurate estimation for the covariance function. Since we know that the coherence time of the rain attenuation is of the order of $10^3 \sim 10^4$ seconds (Note that the corner frequency has been shown to be $10^{-3} \sim 10^{-4}$ Hz in Section 2.3), N can be as large as $10^3 \sim 10^4$ for an accurate estimation. However, in our case, we did not have enough length of data, and we could not increase N up to as much as we wanted.

In our case, the $\hat{K}_{yy}[m]$ is updated each time using the last N data from $y[n-N+1]$ to $y[n]$. Therefore, it would be more rigorous to write (2.18) as follows:

$$\hat{K}_{yy}[m;n] = \frac{1}{N-|m|} \sum_{k=n-N+1}^{n-|m|} y[k]y[k+|m|] \qquad |m| \le N-1 \tag{2.19}$$

$$0 \qquad \text{otherwise.}$$

In summary, our predictor uses N data points to obtain $\hat{K}_{yy}[m]$ and these yield the c_i's at each time n, which are then used to predict $\hat{y}[n+j]$ $(j \ge 0)$ based on the past data $y[n-1]$ and/or $y[n-2]$.

Fig. 2.7 shows the data measured and predicted on a clear day and their prediction errors resulting from the above procedure when $j = 0$ and $j = 3$. We have used a two pole AR model for a prediction equation and the last 10 data points $(N = 10)$ to obtain $\hat{K}_{yy}[m]$ and c_i. Fig 2.8 corresponds to the case of a moderately rainy day with a one pole AR model and $N = 10$.

We can see that in both cases of a clear day and a moderately rainy day, the prediction error is within ± 0.5 dB almost all the time when $j = 0$ and within ± 1.0 dB when $j = 3$. This shows that we can predict the future signal attenuation due to weather on satellite-earth paths with a relatively small error, with one or two past data. This prediction error can be compensated for by providing a fixed power margin large enough to compensate for the possible maximum prediction error.

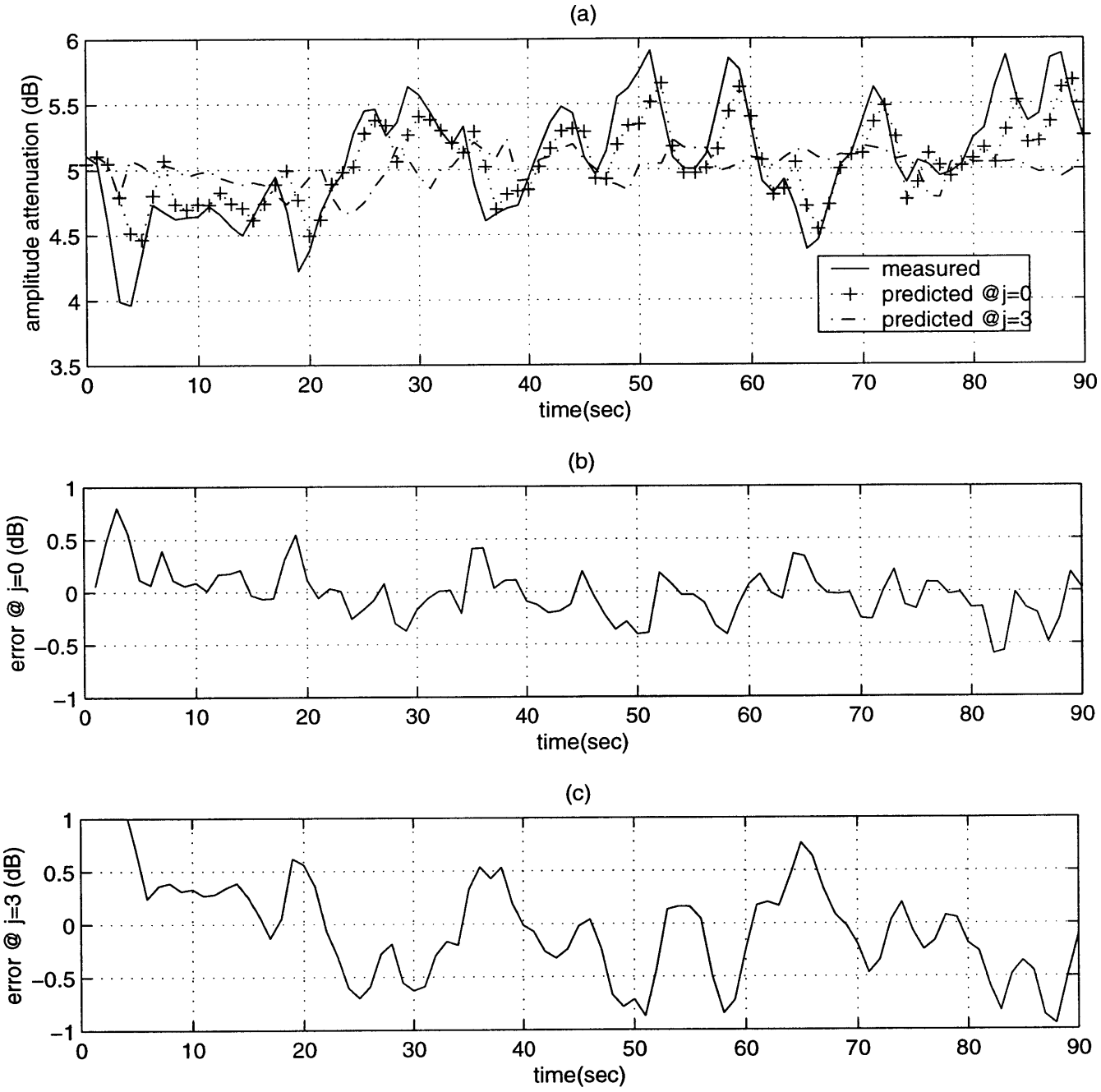

Figure 2.7: (a) Measured and Predicted (when $j = 0$ and $j = 3$) Data on a Clear Day (b) Corresponding Prediction Error when $j = 0$ (c) Corresponding Prediction Error when $j = 3$

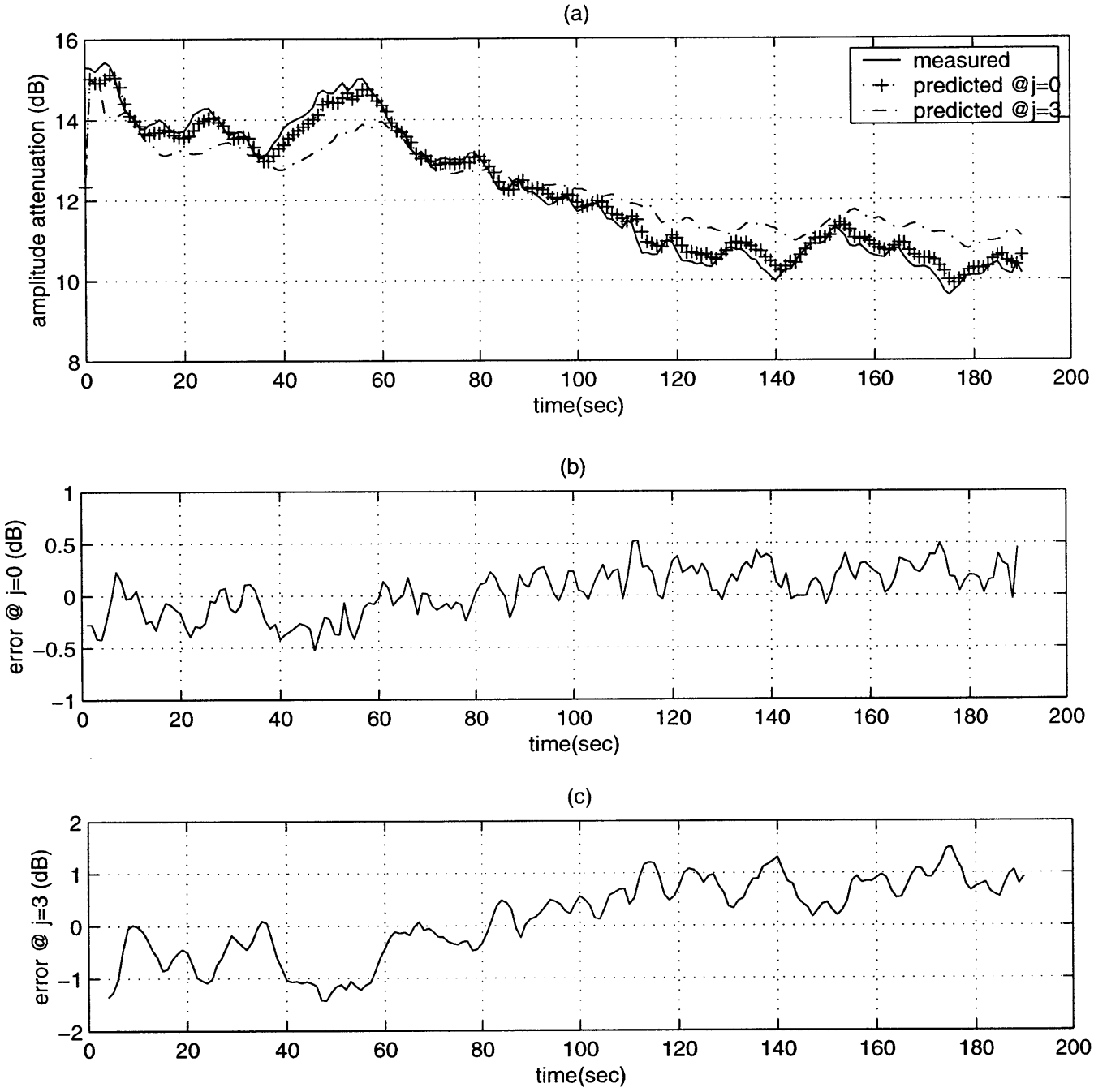

Figure 2.8: (a) Measured and Predicted (when $j = 0$ and $j = 3$) Data on a Moderately Rainy Day (b) Corresponding Prediction Error when $j = 0$ (c) Corresponding Prediction Error when $j = 3$

2.5 Summary

In this chapter, we investigated channel modeling and prediction in satellite-earth communications at high frequencies (above 10 GHz). The major points to highlight are as follows:

- Rain attenuation and received signal scintillation due to atmospheric turbulence dominate the signal attenuation in satellite-earth communications at high frequencies such as Ka-band.

- Both rain attenuation and received signal scintillation can be modeled as lognormal distributions for short durations.

- Rain attenuation has a PSD with a slope of -20 dB/decade and a corner frequency of the order of 10^{-3} ~ 10^{-4} Hz. For scintillation, the PSD has a slope range of -23 ~ -37 dB/decade and a corner frequency of the order of 0.1 Hz.

- We can use a one pole AR model for rain attenuation and a one or two pole AR model for scintillation.

- We can obtain the prediction equation of signal attenuation with only one or two past data points with the prediction coefficients c_i's, which are updated every second using the last N data. In the example in Section 2.4, with $N = 10$, the prediction error is within ± 0.5 dB one second ahead and within ± 1.0 dB four seconds ahead.

In the following chapter, we will explore the various possibilities of channel adaptation, where we will vary the transmission power and the data rate adaptively based on channel modeling and the prediction methods developed in this chapter.

Chapter 3

Channel Adaptation

3.1 Overview

3.1.1 Review of the Previous Chapter

In the previous chapter, we considered channel modeling and prediction for the satellite-earth channel. Scintillation and rain attenuation have been treated as the main causes of signal attenuation over satellite channels with weather-induced impairments. With the knowledge that scintillation can be expressed by a one or two pole AR model and rain attenuation can be expressed by one pole, we have presented results where future signal attenuation, which directly decides the future channel state, can be predicted within ± 0.5 dB 1 second ahead ($j = 0$ in Section 2.4) and within ± 1.0 dB 4 seconds ahead ($j = 3$).

3.1.2 Necessity of Channel Adaptation

Why do we need channel adaptation? As we have seen in the previous chapter on channel modeling and prediction, the satellite channels over high frequencies such as Ka-band exhibit high signal attenuation due to rain, which can be as high as 30 ~ 40 dB. This

causes satellite links to be designed with at least a 10 dB power margin over the requirement when weather conditions are good, so that this margin can prevent data loss due to bad weather conditions. Rain events that yield 20+ dB attenuation are rare enough that the service provider usually will declare the links to be unavailable and include these events into availability guarantees.

If we provide the high extra power margin all the time, power or capacity would be wasted when the link does not need the high margin, e.g., when the path is clear. Thus, channel adaptation by varying the power and/or the data transmission rate according to the channel state will improve efficiency significantly (up to as much as 20 dB's).

3.1.3 Method of Channel Adaptation

With power adaptation, the transmitter will reduce transmitted power during good weather and increase power during bad weather conditions. Or instead of changing the power margin itself, we may adjust the data transmission rate, such that the signal will have just enough power per symbol for reliable detection at the receiver. We can consider a modulation symbol size M and a code rate (the inverse of the amount of redundancy) r as control parameters for the variable data transmission rates. With fixed transmitter power, the data transmission rate is increased in good weather while the rate is decreased in bad weather, so that the transmitted signal can have sufficient power per symbol.

In this work, we consider schemes that use both controls of power and data transmission rates, and in particular, we suggest a *continuous power control and discrete rate control* strategy. We define a finite number of data transmission rate states according to signal attenuation (Fig. 3.1). A specific code rate and a modulation symbol size, which differ from state to state, are assigned to each state. The code rate and the modulation symbol

size in each state are designed to be appropriate for the signal attenuation interval of that state, to yield the bit error rate (BER) less than or equal to a target BER. When signal attenuation is predicted to cross over the boundary between different states, we will implement a discrete change of the code rate and/or the modulation symbol size. Within each state, continuous power control is implemented in every second to compensate for signal attenuation over satellite-earth paths, so as to keep a received signal-to-noise ratio (SNR) constant (Note that each state has a different SNR, in general, according to the assigned modulation/coding scheme) for the desired target BER. This strategy keeps the corresponding data transmission rate adapted to yield the target BER of the satellite link, regardless of channel conditions. Through this strategy, we can improve vastly both data throughput and power utilization. In Section 3.3 and 3.4, we will discuss how the boundaries α_i's are set.

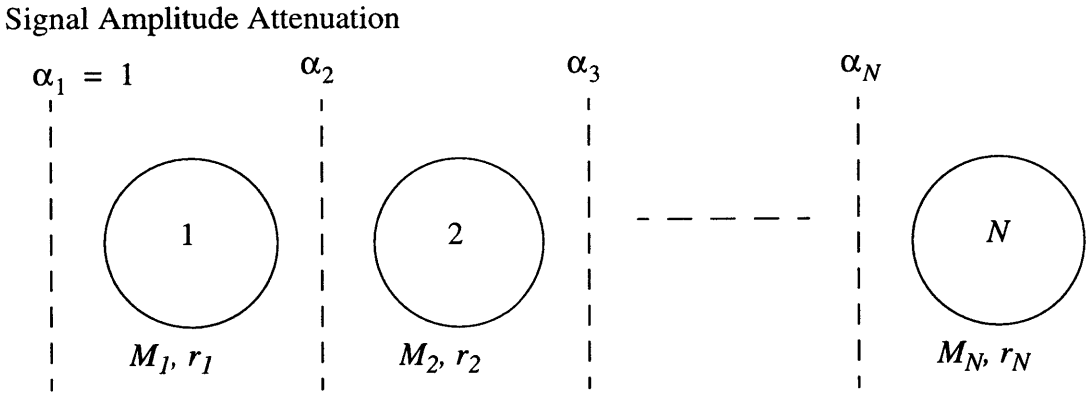

Figure 3.1: Data Rate States: Each state i has boundaries of α_i and α_{i+1}, $(\alpha_{i+1} > \alpha_i \geq 1)$, a modulation symbol size M_i, and a code rate r_i.

3.2 Power Control

Adaptive power control in satellite communications refers to the process of varying transmitter power on a satellite link, mainly in the presence of rain attenuation, to maintain a desired power level at the receiver by increasing the transmitter power during a rain attenuation event, then reducing power after the rain event is over [10]. However, it is desirable to keep the transmitter power at the minimum acceptable level just necessary to overcome rain attenuation under an upper limit to avoid interference to other terminals. Also, it is required to consider nonlinear effects such as back-off and saturation of power amplifiers in satellite communications, which make the application of amplitude modulations, such as quadrature amplitude modulation (QAM), more complicated.

We can consider power control for uplink, downlink, or both. There are two ways to implement power control [10]:

(a) closed loop

(b) open loop.

In closed loop implementations, after monitoring a received signal power level, the receiver tells the transmitter to increase or decrease transmit power accordingly. With open loop power control, the transmitter monitors the received power on the return link, infers the forward link fade, and adjusts its transmit power accordingly. In satellite systems, there are round-trip delays that are not negligible (in particular, for the geostationary earth orbits (GEO) systems). Thus, for fast adaptation (less than 1 second scale), the closed loop system is sometimes inappropriate and more complex. In this case, usually the open loop implementations are preferred although the results in this section are perfectly valid for closed loop systems. In the case that the transmit and the receive frequen-

cies are far apart, channel reciprocity does not hold and a closed loop system should be used.

In this work, we use a *continuous power control* strategy. As stated in Section 3.1, we make a finite number of data transmission rate states, each of which has an upper and a lower boundary, which will be explained in detail in the following sections. In each state, there is a required SNR to assure a target BER with a given modulation and a coding scheme. To compensate for the attenuation of the transmitted signal over satellite-earth paths, we predict signal attenuation and provide more or less power accordingly in advance. This not only achieves the target BER by providing the required SNR, but simplifies our analysis of the BER since continuous power control fixes the SNR operation point. As a consequence, the channel will appear to be a constant attenuation AWGN channel and we need not consider the lognormality of the received signal attenuation in the BER calculation. In other words, if there were no continuous power control, we would have to consider lognormal statistics of the amplitude in our analysis of BER, which would turn out to be as follows:

$$\bar{P}_{e,i} = \left(\int_{\alpha_i}^{\alpha_{i+1}} P_e\left(\frac{SNR_0}{\alpha^2}\right) p_\alpha(\alpha) d\alpha \right) \Big/ \left(\int_{\alpha_i}^{\alpha_{i+1}} p(\alpha) d\alpha \right), \tag{3.1}$$

where $\bar{P}_{e,i}$: average BER in state *i*,

$P_e\left(\frac{SNR_0}{\alpha^2}\right)$: BER of the received signal with the attenuated SNR equal to SNR_0/α^2,

$p_\alpha(\alpha)$: PDF of received signal amplitude attenuation α (lognormal distribution), which is defined to be larger than 0,

SNR_0: originally transmitted SNR at the source, and

α_{i+1}, α_i: upper and lower received signal attenuation boundaries of state i respectively.

On the contrary, if we fix our received SNR at SNR_0/α_i^2 by using continuous power control, we can get

$$\bar{P}_{e,i} = P_e\left(\frac{SNR_0}{\alpha^2_i}\right), \tag{3.2}$$

which gives better performance than (3.1). This is illustrated in Fig. 3.2.

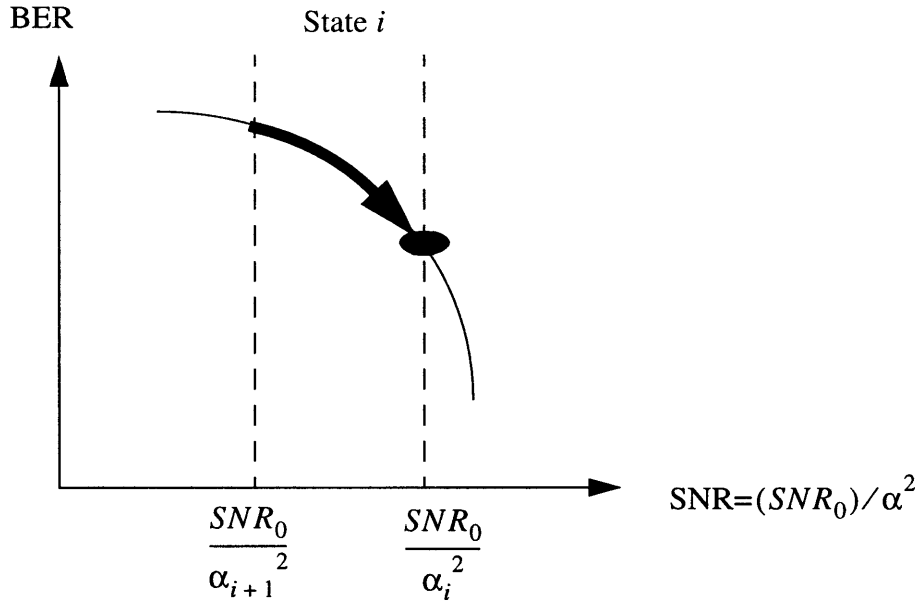

Figure 3.2: Description of Continuous Power Control: By using continuous power control, we fix our received SNR at SNR_0/α_i^2 ($\alpha_{i+1} > \alpha_i \geq 1$).

3.3 Rate Control

In all modern digital communications, coding and modulation techniques are being used for more efficient and reliable data transmissions. These two techniques affect the relation between the SNR and the BER, which are the parameters that we are concerned with in this work. Also, coding and modulation techniques determine the data transmission rate, which should be considered as another important parameter in our system and will be explored in this section.

A digital modulator produces analog waveform signals according to a sequence of discrete symbols from a finite number, say M, of alphabets $\{0, 1,..., M-1\}$, into which binary digits from a source or a coder are mapped [11]. If we implement only modulation symbol size adaptation, we will change M as α^2 changes with the corresponding power adjustment to yield the target BER. The required level of the received SNR = SNR_0/α^2 will be a monotonically increasing function of the modulation symbol size M. Therefore, we will increase M in fine weather conditions to increase data rate and reduce M to reduce data rate in bad weather conditions.

The simplest scheme to implement for M-ary modulation in a satellite channel is M-ary phase shift keying (M-PSK), which is easy to analyze since all symbols have equal symbol energy and equal number of nearest neighbor signals. However, in satellite communications, since both power and bandwidth are the most important resources, bandwidth efficient modulations (BEM) such as M-ary quadrature amplitude modulation (M-QAM) are being considered for use. The nonlinearity of the satellite channel and the amplitude and phase modulation (AM and PM) characteristic of BEMs require the use of

equalization to eliminate memory over the received symbols and intersymbol interference, resulting in rather complex system designs.

We can also reduce the amount of required transmitter power for the target BER through the use of forward error correction (FEC) coding [12]. This is achieved at the cost of increased bandwidth since more coded bits are assigned to information bits for error detection and/or correction. The ratio of the number of information bits to that of coded bits is called a *code rate*. The smaller a code rate is, the larger the required bandwidth. There are two types of codes widely used: block codes and convolutional codes. A systematic block encoder adds parity bits to a block of information bits to form a codeword. Parity bits are decided according to linear combinations of an incoming block of information bits. A convolutional code uses shift registers and adders, which generate coded bits from a segment (whose length is called a constraint length) of information bits. It is known that the optimal decoding method for convolutional codes is the Viterbi algorithm. In either a block or convolutional coding scheme with a variable code rate, when the channel condition is good, we will increase the code rate close to 1, which corresponds to uncoded transmission, while we decrease the rate in more fading conditions to provide more coded bits, and thus more diversity.

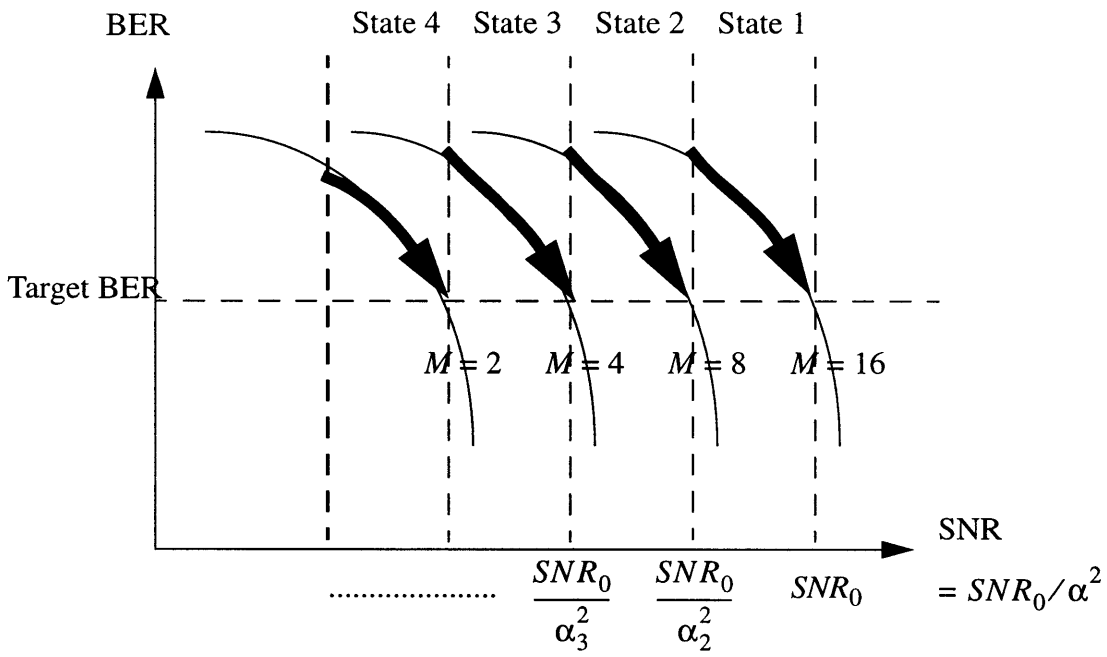

Figure 3.3: Description of Continuous Power Control and Discrete Rate Control

In our work, we consider change of both the modulation symbol size and the code rate. Our strategy of *continuous power control and discrete rate control* is illustrated in Fig. 3. 3. For the target BER, we make use of a discrete number of states, each of which has its own specific modulation symbol size M and code rate r. And each state corresponds to one of BER-SNR curves within an interval in Fig. 3.3. We divide the SNR, which is expressed as SNR_0/α^2 in our case, into a discrete number of intervals, whose boundaries are determined to secure the target BER. And within the interval from α_i to α_{i+1}, by using continuous power control, we move the operation point to the optimal point, SNR_0/α_i^2.

3.4 Examples

In this section, we show some examples using different modulation and/or coding schemes to illustrate our channel adaptation strategy.

3.4.1 Uncoded *M*-PSK Modulation

In *M*-PSK [13], during each signaling interval of duration *T*, one signal is sent from a set of *M* possible signals

$$s_i(t) = \sqrt{\frac{2E_s}{T}}\cos\left(2\pi f_c t + \frac{2\pi}{M}(i-1)\right) \qquad i = 1, 2, \ldots, M \tag{3.3}$$

where E_s is the signal energy per symbol, and f_c is the carrier frequency. This can be shown in a signal-space diagram as in Fig. 3.4.

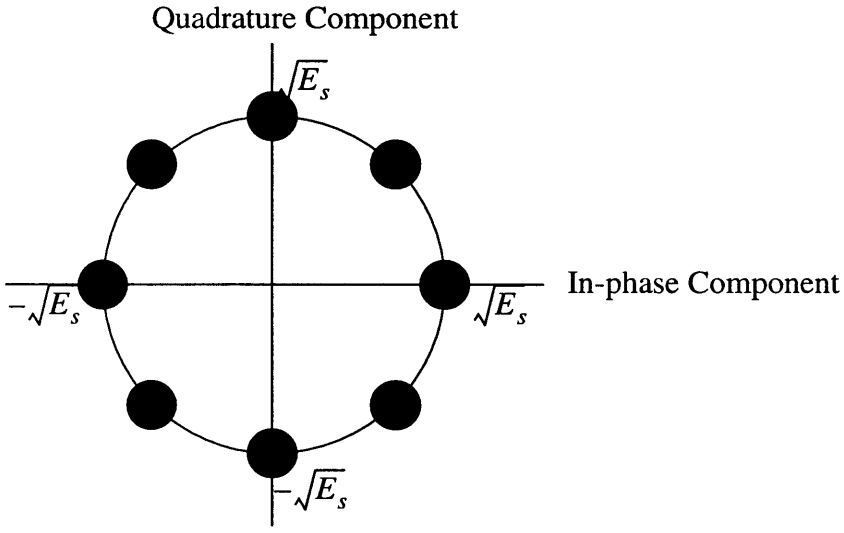

Figure 3.4: Signal-Space Diagram of *M*-PSK (*M* = 8)

For a simple analysis of M-PSK in channel adaptation schemes, we assume coherent detection over channels with additive white Gaussian noise (AWGN), whose mean is zero and variance is $N_0/2$, and use the following approximations, which yield simple average probability of symbol error. By using the union of events bound and considering only two nearest neighbor signals, the average probability of symbol error P_e of uncoded M-PSK signal is

$$P_e \le 2Q\left(\sqrt{2 \cdot \frac{E_s}{N_0} \cdot \frac{1}{\alpha^2}} \cdot \sin\left(\frac{\pi}{M}\right)\right), \tag{3.4}$$

where E_s is the signal energy per symbol, α is the amplitude attenuation of the received signal defined to be larger than 0, and $Q(x)$ is a Q-function, $Q(x) = \frac{1}{\sqrt{2\pi}} \int_x^\infty e^{-u^2/2} du$.

Using the upper bound of the Q-function, $Q(x) < \frac{1}{2}\exp\left(-\frac{1}{2}x^2\right)$, we get

$$P_e \le \exp\left(-\frac{E_s}{N_0} \cdot \frac{1}{\alpha^2} \cdot sin^2\left(\frac{\pi}{M}\right)\right). \tag{3.5}$$

The BER P_b is less than the symbol error rate P_e. Thus, if the target BER is P_b^*,

$$P_b \le P_e \le \exp\left(-\frac{E_s}{N_0} \cdot \frac{1}{\alpha^2} \cdot sin^2\left(\frac{\pi}{M}\right)\right) \le P_b^* \ . \tag{3.6}$$

Solving this for α^2 with the equality gives the lower boundary of the state i, α_i^2, for each $M = 2, 4, 8, ...,$

$$\alpha_i^2 = \left(\frac{E_s/N_0}{\ln(1/P_b^*)} \cdot sin^2\left(\frac{\pi}{M}\right)\right). \tag{3.7}$$

If we try $E_s/N_0 = 25$ dB and $P_b^* = 10^{-8}$, we have

$$\alpha_i^2 = 17.2 \cdot sin^2\left(\frac{\pi}{M}\right), \tag{3.8}$$

and Table 3.1 shows the state boundaries of the signal power attenuation for each $M = 2, 4, 8, \ldots$ in this case.

M	α_i^2
2	12.3 dB
4	9.3 dB
8	4.0 dB

Table 3.1: M vs. α_i^2 Relation of M-PSK

Therefore, in this case, we can build four states according to the boundaries of power attenuation given in Table 3.1:

State 1: 0.0 ~ 4.0 dB (16PSK)

State 2: 4.0 ~ 9.3 dB (8PSK)

State 3: 9.3 ~ 12.3 dB (4PSK)

State 4[1]: 12.3 ~ 12.3 + x dB (BPSK).

With this scheme ($E_s/N_0 = 25$ dB and $P_b^* = 10^{-8}$), we can obtain the coverage of the received signal power attenuation up to 12.3 dB to provide the data rate of more than 1 bits/s based on adapting the modulation symbol size alone.

1. The upper boundary of the last state, State 4, is determined by the maximum power compensation margin that the system can endure before reaching the saturation point. In this case, the transmitter can provide at most 25 + x dB power, where x is determined in the specific system.

3.4.2 Uncoded *M*-QAM Modulation

While the *M*-PSK scheme modulates just the signal phase keeping the signal envelope constant, in an *M*-QAM system [13], we use amplitude modulation as well as phase modulation to gain more efficiency albeit at the expense of considerably more complexity. The transmitted signal of the *M*-QAM scheme during each signaling interval of duration T is

$$s_i(t) = \sqrt{\frac{2E_0}{T}}a_i\cos(2\pi f_c t) + \sqrt{\frac{2E_0}{T}}b_i\sin(2\pi f_c t) \qquad i = 1, 2, \ldots, M, \tag{3.9}$$

where E_0 is the energy of the signal per symbol with the lowest amplitude, and a_i and b_i are a pair of independent integers chosen according to the location of the signal in a signal-diagram space, which is shown in Fig. 3.5.

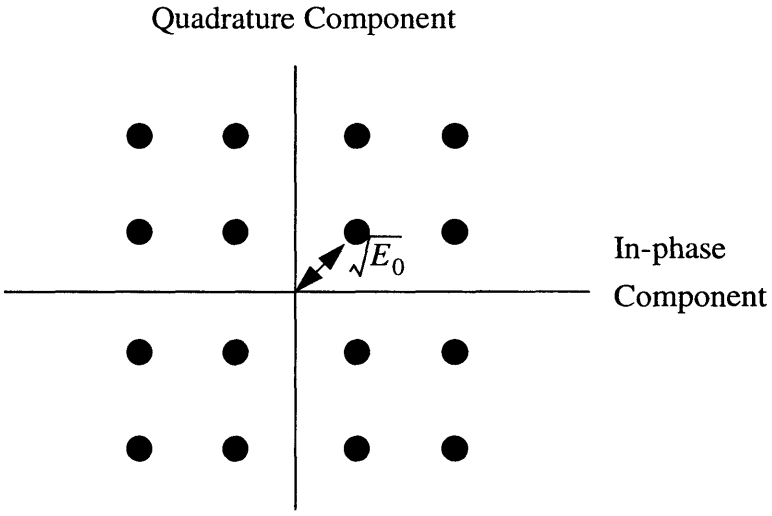

Figure 3.5: Signal-Space Diagram of *M*-QAM ($M = 16$)

As in the case of M-PSK, for a simple analysis, we assume coherent detection over zero-mean and $N_0/2$-variance AWGN channels and use similar approximations as we did in 3.4.1. Using the fact that in-phase and quadrature components are independent and each component has a geometry of $\sqrt{M}$-ary pulse-amplitude modulation (PAM), we have the average probability of symbol error of uncoded M-QAM,

$$P_e \approx 4Q\left(\sqrt{\frac{3}{M-1}\cdot\frac{E_{av}}{N_0}\cdot\frac{1}{\alpha^2}}\right), \tag{3.10}$$

where $E_{av} = \dfrac{2(M-1)E_0}{3}$ is the average signal energy per symbol.

Using the upper bound of the Q-function, we get

$$P_e \le 2\exp\left(-\frac{3}{2}\cdot\frac{E_{av}}{N_0}\cdot\frac{1}{\alpha^2}\cdot\frac{1}{M-1}\right). \tag{3.11}$$

With the target BER, P_b^*, (3.11) should be less than P_b^*. Solving for α^2 with the equality gives the lower boundary of the state i, α_i^2, for each $M = 2, 4, 16, \ldots$,

$$\alpha_i^2 = \frac{3}{2}\cdot\frac{E_{av}/N_0}{\ln(2/P_b^*)}\cdot\frac{1}{M-1}. \tag{3.12}$$

If we try $E_{av}/N_0 = 25$ dB and $P_b^* = 10^{-8}$, we have

$$\alpha_{i-1}^2 = \frac{24.8}{M-1}, \tag{3.13}$$

and Table 3.2 shows the state boundaries of signal power attenuation for each $M = 2, 4, 16, \ldots$

M	α_i^2
2	13.9 dB
4	9.2 dB
16	0.22 dB

Table 3.2: M vs. α_i^2 Relation of M-QAM

Therefore, in this case, we can make four states like in 3.4.1:

State 1: 0.0 ~ 0.22 dB (64-QAM)

State 2: 0.22 ~ 9.2 dB (16-QAM)

State 3: 9.2 ~ 13.9 dB (4-QAM)

State 4[1]: 13.9 ~ 13.9 + x dB (2-QAM (= BPSK)).

With this scheme (E_{av}/N_0 = 25 dB and P_b^* = 10^{-8}), we can obtain the coverage of the received signal power attenuation up to 13.9 dB to provide the data rate of more than 1 bits/s, slightly better than the M-PSK scheme.

3.4.3 Rate - (n-1)/n Punctured Convolutional Codes

In Section 3.3, we briefly addressed convolutional codes. Here, we introduce puncturing in order to make the code rate high and easy to vary. A punctured convolutional code [14] is a higher-rate code obtained by periodic elimination (i.e., puncturing) of specific code symbols from the output of a lower-rate convolutional encoder. By an appropriate choice

1. As in the case of M-PSK in 3.4.1, we assume that the transmitter can provide maximum 25 + x dB power, and the upper boundary of the last state is determined accordingly.

of the original lower-rate code and the perforation pattern, any rate code may be obtained. Fig. 3.6 shows a typical punctured convolutional encoder.

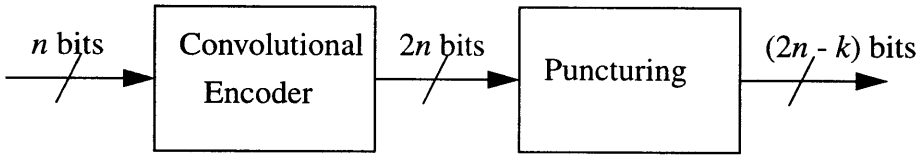

Figure 3.6: Punctured Convolutional Encoder: A rate-1/2 encoder and a puncturer provide a rate-$n/(2n - k)$ code.

When Viterbi decoding is performed for such a punctured code, which is rate-$(n\text{-}1)/n$ and derived from a rate-1/2 code, the upper bound of the bit error probability is given by [15]:

$$P_b \leq \sum_{k=d}^{\infty} \tilde{C}_k P_k \cong \tilde{C}_d P_d, \tag{3.14}$$

where d is the minimum free distance of the punctured code, $\tilde{C}_k$ is the normalized total number (per each information bit) of error bits produced by all incorrect paths with distance k from the correct path at each of n-bit blocks of the original code, and P_k is the probability that one such incorrect path is selected in the Viterbi decoding process. The approximate equality in (3.14) comes from the assumption that the error at the minimum free distance is dominant. When BPSK modulation with coherent detection over the zero-mean and $N_0/2$-variance AWGN channel is assumed,

$$P_d = Q\left(\sqrt{2d \cdot r \cdot \frac{E_b}{N_0} \cdot \frac{1}{\alpha^2}}\right) \leq \frac{1}{2}\exp\left(-d \cdot r \cdot \frac{E_b}{N_0} \cdot \frac{1}{\alpha^2}\right) \tag{3.15}$$

where r is the code rate $(n - 1)/n$, E_b is the signal energy per bit (equal to the signal energy per symbol since we use BPSK in this case) and the inequality follows from the upper bound of the Q-function.

With the target BER P_b^*, we have

$$P_b \le \tilde{C}_d P_d \le \frac{1}{2}\tilde{C}_d \exp\left(-d \cdot r \cdot \frac{E_b}{N_0} \cdot \frac{1}{\alpha^2}\right) \le P_b^*. \tag{3.16}$$

Solving this for α^2 gives

$$\alpha^2 \le \frac{d \cdot r \cdot E_b/N_0}{\ln(\tilde{C}_d/(2P_b^*))}, \tag{3.17}$$

where we have three variables, d, r, and $\tilde{C}_d$ dependent on a specific coding scheme. Here, we use the punctured codes derived from a rate-1/2 convolutional code with a constraint length (the number of registers when we generate a convolutional code) equal to 6 in [15]. d and $\tilde{C}_d$ for punctured codes are provided in Table 3.3.

Rate	1/2	2/3	3/4	4/5	5/6	6/7	7/8	8/9	9/10	10/11	11/12	12/13	13/14
d	10	6	5	4	4	3	3	3	3	3	3	3	3
$\tilde{C}_d$	36	1.5	14	3	18.4	0.8	1.3	1.6	3.2	5.2	6	6.9	16.5

Table 3.3: d and $\tilde{C}_d$ for Punctured Codes [15]

If we try $E_b/N_0 = 25$ dB and $P_b^* = 10^{-8}$ with these punctured codes and BPSK modulation[1], we have Fig. 3.7, where the lower boundary for each code rate $(n - 1)/n$ is shown.

1. Uncoded BPSK scheme has been shown to have the lower boundary of 12.3 dB of signal attenuation in Table 3.1. We can see this again in the case of rate 1 in Fig. 3.7.

We can see that the coding gain of rate-1/2 code is about 6 dB, which is a good agreement with Table 8.1 in [16].

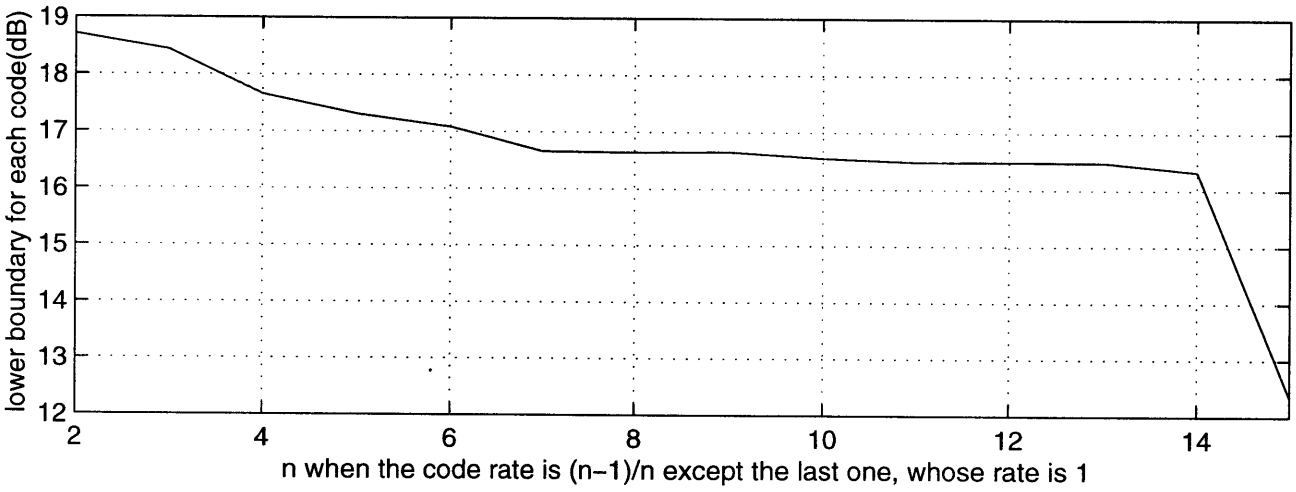

Figure 3.7: Lower Boundaries for Punctured Codes in [15]

3.4.4 Trellis-Coded Modulation

Trellis-coded modulation (TCM) [11, 13] treats modulation and coding as a combined entity rather than as two separate operations. The design of TCM involves the notion of *set partitioning*, by which we partition the original signal set into equal-sized disjoint subsets and partition these subsets again into smaller ones. As a consequence, the minimum Euclidean distance between the signal points in a subset is maximized in maximum likelihood soft-decision decoding in the presence of AWGN, which results in an additional coding gain of TCM. For example, 8PSK is partitioned into two disjoint QPSK subsets, and each QPSK subset is partitioned again into two disjoint BPSK subsets, so that we can

obtain the minimum Euclidean distance between signal points in BPSK, $2\sqrt{E_s}$, where E_s is the signal energy per symbol, instead of that in 8PSK, $\sqrt{2-\sqrt{2}}\sqrt{E_s}$. A typical trellis code encoder is shown in Fig. 3.8. Coded bits from the convolutional encoder select a subset and remaining uncoded bits select a signal point from the subset.

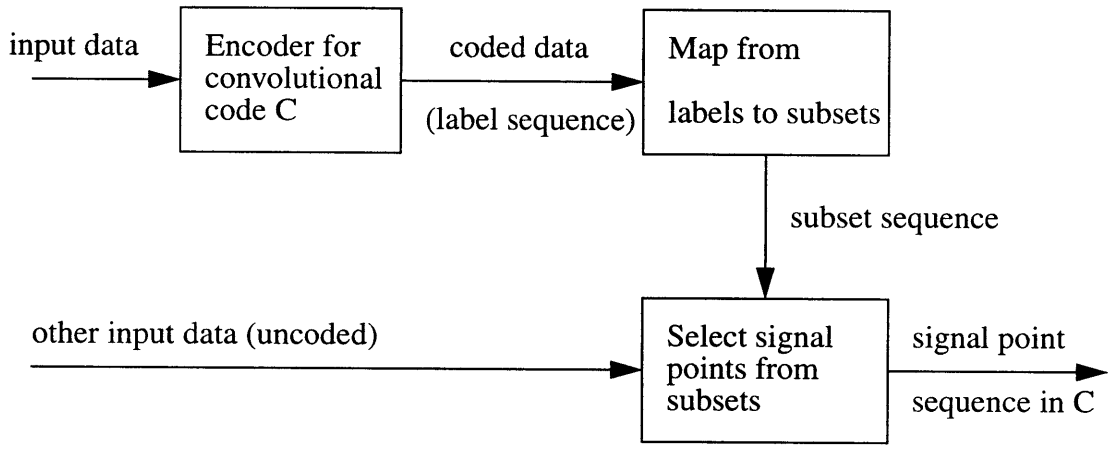

Figure 3.8: Trellis Code Encoder [16]

[11] shows the coding gains that can be obtained by using some TCMs as follows:

rate-1/2 4-state QPSK: 4.0 dB (compared to uncoded BPSK)

rate-2/3 4-state 8PSK: 3.0 dB (compared to uncoded QPSK)

rate-3/4 8-state 16QAM: 4.4 dB (compared to uncoded 8PSK).

The coding gains have been obtained through comparisons between a TCM and an uncoded scheme, both of which have the same number of transmitted bits per symbol. For example, the first pair of rate-1/2 4-state QPSK and uncoded BPSK has 1 bit/symbol transmission while the second and the third pair have 2 and 3 bits/symbol respectively.

When we combine these TCM coding gains with the lower boundaries of the states in Table 3.1, we can get new state boundaries of the received signal attenuation in Table 3.4, where the adaptation with TCM has been considered.

	α_i^2
rate-1/2 4-state QPSK	16.3 dB (= 12.3 + 4.0)
rate-2/3 4-state 8PSK	12.3 dB (= 9.3 + 3.0)
rate-3/4 8-state 16QAM	8.4 dB (= 4.0 + 4.4)

Table 3.4: Lower Boundaries for the Adaptive TCM Scheme

However, we believe that this scheme is not practical since each TCM scheme has its own different hardware implementation, so that the switches among them are not so easy.

3.5 Performance Evaluation

In Section 3.4, we showed several examples, where we built a set of modulation/coding states according to the received signal attenuation for channel adaptation. In this section, we will show how much improvement we can get for channel utilization when we use the channel adaptation scheme developed so far.

3.5.1 Parameters for Performance Evaluation

There are several parameters that should be considered for comparison between the adaptive scheme and the non-adaptive scheme.

Availability

The quality of service (QoS) over a communication link can be evaluated by the *availability* or the *outage*. The availability is defined as the probability that a variable, such as the BER or the SNR, is in the region of the desired levels. The availability is sometimes also called the reliability. The outage or the exceedance is defined to be equal to 1 - availability. For example, with the BER and its target probability of error P_b^*, the availability P_{avl} can be expressed by

$$P_{avl} = Pr\{BER \leq P_b^*\}. \tag{3.18}$$

Average Rate

In adaptive rate control systems, the data rate changes as the modulation symbol size M and/or the code rate r vary adaptively according to the amplitude attenuation α of the received signal. If $R(\alpha)$ denotes the data rate when the amplitude attenuation of the received signal is equal to α, the average rate $E[R]$ is given by

$$E[R] = \int_0^\infty R(\alpha) p_\alpha(\alpha) d\alpha, \tag{3.19}$$

where $p_\alpha(\alpha)$ is the PDF of α.

Average Power Increase

Similar to the case of adaptive data rate systems, in adaptive power control systems, the power increase added to the initial transmitter power changes adaptively accord-

ing to the received signal attenuation α. When the required power increase for signal attenuation α is denoted by $\Delta(\alpha)$, the average power increase $E[\Delta]$ is given by

$$E[\Delta] = \int_0^\infty \Delta(\alpha) p_\alpha(\alpha) d\alpha, \tag{3.20}$$

where $p_\alpha(\alpha)$ is the PDF of α.

3.5.2 Ideal Case

Let us compare the adaptive scheme with the non-adaptive scheme under the ideal assumption that we have a 'genie-aided' sensing system that can tell the exact future value of the received signal attenuation. This implies that we have a perfect prediction method, which makes no prediction error at all. Then, with our continuous power control and discrete rate control scheme, we can get rate, required power increase, and BER vs. received signal attenuation relations as shown in Fig. 3.9. We assume that we choose the initial transmitter power to assure the highest rate R_1 with the target BER when there is no signal attenuation. Thus, the required power increase in Fig. 3.9 is just an additional power amount over the initial power. In all states including the last one, the upper boundary is determined by the maximum power compensation that the system can tolerate before reaching the saturation point.

Whereas, with the non-adaptive scheme that has a fixed data rate R_N with a fixed modulation/coding scheme and provides a fixed power margin all the time, we can get the corresponding relations in Fig. 3.10. In order to obtain the same availability as in the adaptive scheme, the non-adaptive scheme must have the same channel-off turn-point as the adaptive scheme does. This can be achieved by providing over all attenuation levels the fixed

power margin that is equal to the maximum power margin of the adaptive scheme, which results in waste of the power resource.

In addition, the fixed margin has been chosen to assure just the lowest rate R_N in the worst attenuation level. Thus, if only one data rate is provided in the non-adaptive scheme, that rate cannot be larger than R_N, which results in inefficiency in terms of data rate, and hence, channel utilization.

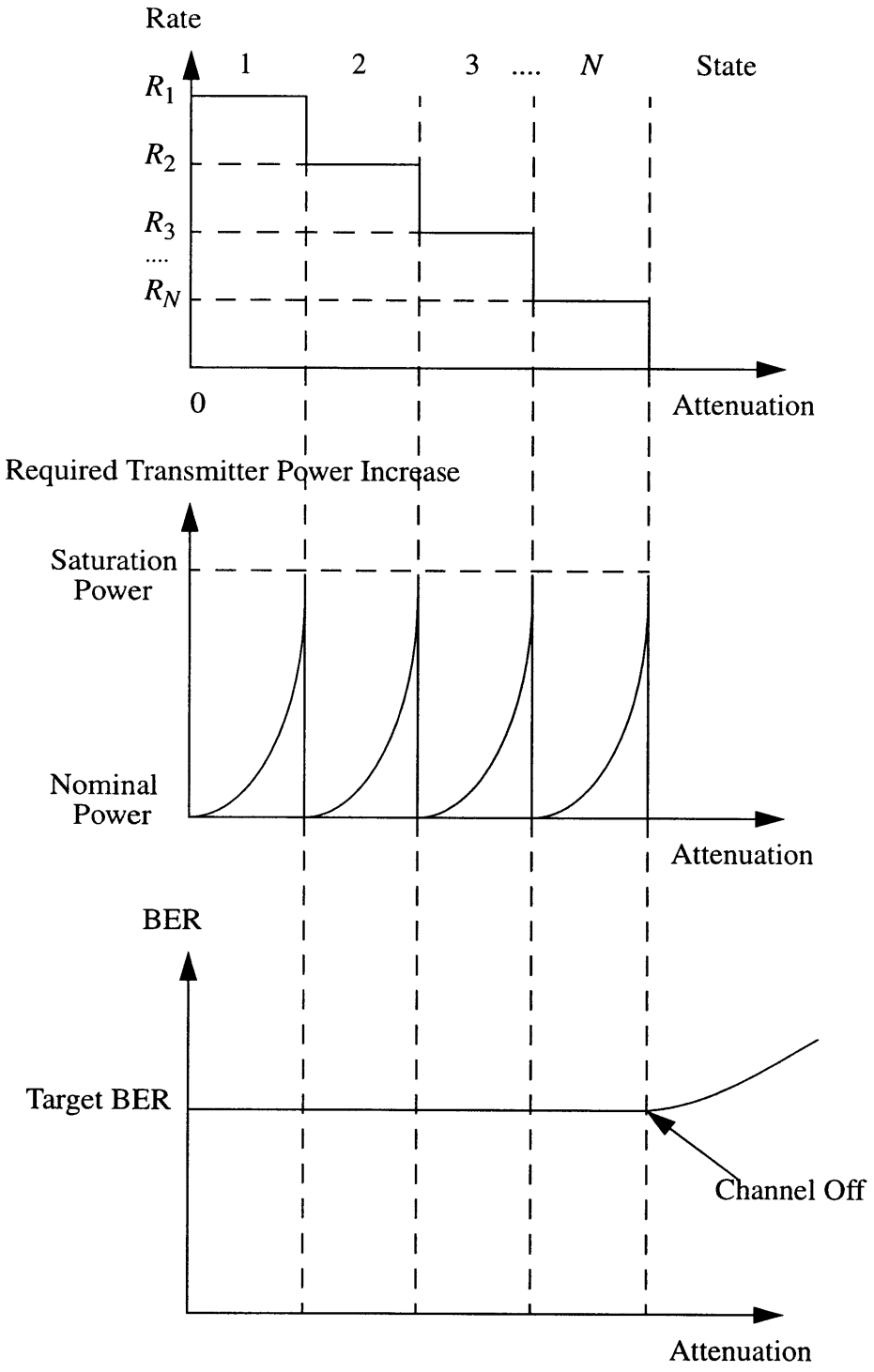

Figure 3.9: Rate, Required Transmitter Power Increase, and BER vs. Attenuation in the Adaptive Scheme

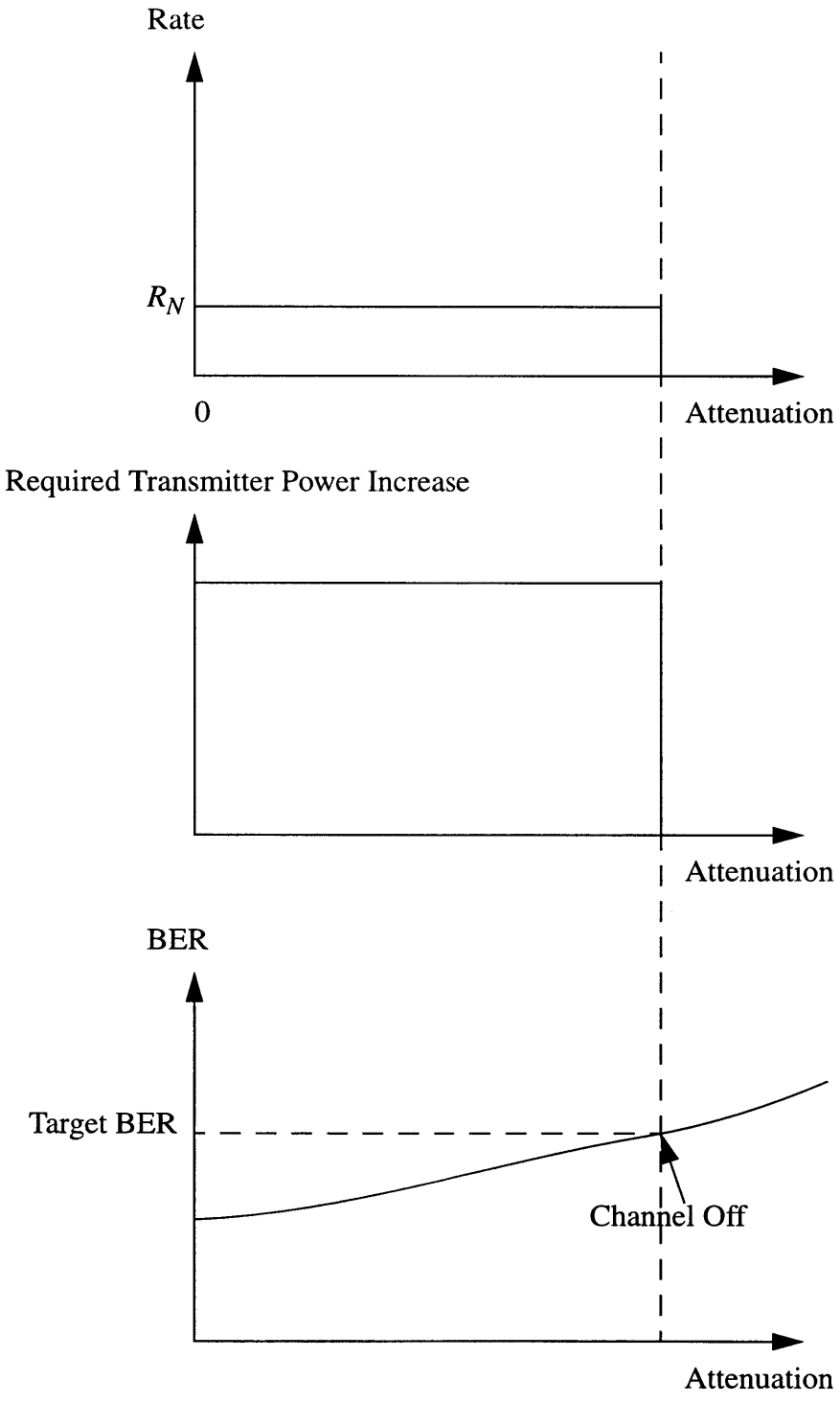

Figure 3.10: Rate, Required Transmitter Power Increase, and BER vs. Attenuation in the Non-Adaptive Scheme

3.5.3 Analysis of Power Increase

We now analyze the amount of power increase in comparing the non-adaptive and the adaptive scheme.

With Adaptive Power Control Only

Let us make a comparison between the average power increase of the non-adaptive scheme and that of the adaptive scheme with adaptive power control only.

Fig 3.11 shows the relation of the received signal energy and signal attenuation for both schemes. We assume that both schemes have the same fixed data rate. L denotes the value of α when the channel turns off. E_0 is the initial transmitter signal energy to yield the given data rate at a given target BER. μ^* is the fixed

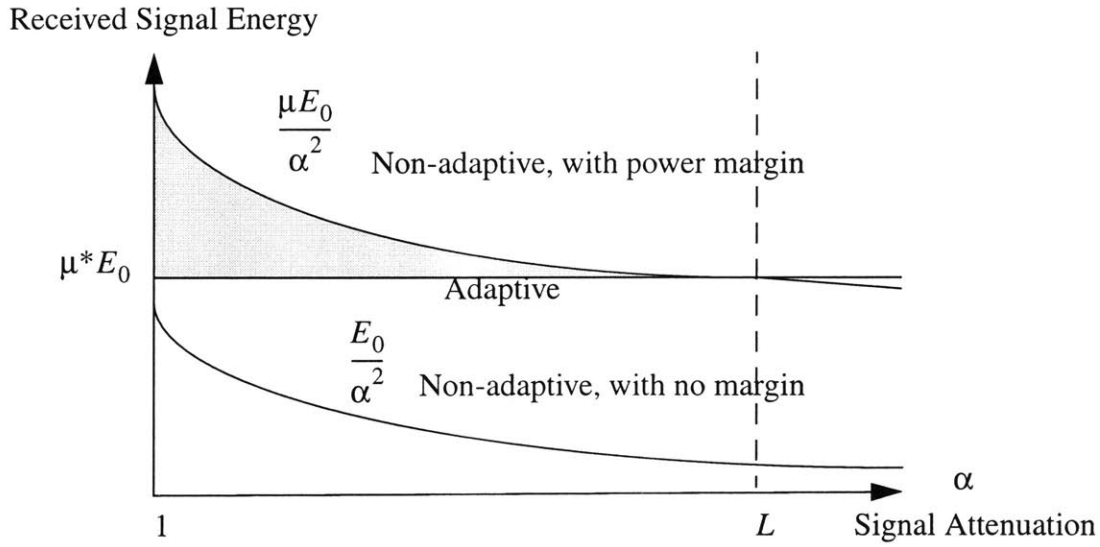

Figure 3.11: Relation between the Received Signal Energy and Signal Attenuation for the Adaptive (with Power Control Only) and the Non-adaptive Scheme

small power margin provided to compensate for the prediction error in the adaptive scheme. μ is the fixed power margin in the non-adaptive scheme, and is selected so that both schemes have the same signal energy at $\alpha = L$ for the same data rate.

Then, the average power increase of the non-adaptive scheme is

$$E[\Delta_{non-ad}] = \int_0^L \left(\mu\frac{E_0}{\alpha^2} - \frac{E_0}{\alpha^2}\right) p_\alpha(\alpha)d\alpha, \tag{3.21}$$

where we define the range of signal attenuation α to be larger than 0 with the same reason as in 2.2.2.

The average power increase of the adaptive scheme is

$$E[\Delta_{ad}] = \int_0^L \left(\mu^* E_0 - \frac{E_0}{\alpha^2}\right) p_\alpha(\alpha)d\alpha. \tag{3.22}$$

Therefore, the power gain G by using the adaptive scheme represented by the shaded region in Fig. 3.11 is

$$\begin{aligned} G &= \frac{E[\Delta_{non-ad}] - E[\Delta_{ad}]}{E_0} \\ &= \int_0^L \left(\frac{\mu}{\alpha^2} - \mu^*\right) p_\alpha(\alpha)d\alpha \\ &= \int_0^\infty \left(\frac{\mu}{\alpha^2} - \mu^*\right) p_\alpha(\alpha)d\alpha - \int_L^\infty \left(\frac{\mu}{\alpha^2} - \mu^*\right) p_\alpha(\alpha)d\alpha. \end{aligned} \tag{3.23}$$

The first term of G is

$$\int_0^\infty \left(\frac{\mu}{\alpha^2} - \mu^*\right) p_\alpha(\alpha)d\alpha = \mu\overline{\left(\frac{1}{\alpha^2}\right)} - \mu^*, \tag{3.24}$$

where with $\ln\alpha = z$, $E[z] = \ln m$, and $\mathrm{var}(z) = \sigma^2$,

$$\begin{aligned}
\overline{\left(\frac{1}{\alpha^2}\right)} &= \int_0^\infty \frac{1}{\alpha^2} p_\alpha(\alpha)\,d\alpha \\
&= \int_{-\infty}^{\infty} e^{-2z} \frac{1}{\sqrt{2\pi\sigma^2}} e^{-\frac{(z-\ln m)^2}{2\sigma^2}}\,dz \\
&= \int_{-\infty}^{\infty} \frac{1}{\sqrt{2\pi\sigma^2}} e^{-\frac{(z-\ln m+2\sigma^2)^2}{2\sigma^2}} e^{2\sigma^2-2\ln m}\,dz \\
&= e^{2\sigma^2-2\ln m} \\
&= \frac{1}{m^2}\cdot e^{2\sigma^2}. \qquad (3.25)
\end{aligned}$$

Lower and upper bounds of the second term in equation (3.23) are

$$0 \le -\int_L^\infty \left(\frac{\mu}{\alpha^2} - \mu^*\right) p_\alpha(\alpha)\,d\alpha \le \int_L^\infty \mu^* p_\alpha(\alpha)\,d\alpha \qquad (3.26)$$

with $\alpha = L$ and $\alpha = \infty$ respectively for μ/α^2.

Since $\int_L^\infty \mu^* p_\alpha(\alpha)\,d\alpha = \mu^* \cdot Pr\{\alpha \ge L\}$, we can get

$$\left(\mu\frac{1}{m^2}e^{2\sigma^2} - \mu^*\right) \le Q \le \left(\mu\frac{1}{m^2}e^{2\sigma^2} - \mu^*\right) + \mu^* \cdot Pr\{\alpha \ge L\}, \qquad (3.27)$$

where $Pr\{\alpha \ge L\} = 1 - Pr\{\alpha \le L\}$ is the outage, i.e., 1 - availability of the channel, and

$$\begin{aligned}
Pr\{\alpha \ge L\} &= erfc\left(-\frac{-\ln L + 2\sigma^2}{2\sigma}\right) \\
&\le -\frac{2\sigma}{\sqrt{2\pi}(-\ln L + 2\sigma^2)} \exp\left(-\frac{(-\ln L + 2\sigma^2)^2}{8\sigma^2}\right), \qquad (3.28)
\end{aligned}$$

for $e^{2\sigma^2} \le L < \infty$

where σ^2 is the log amplitude variance and erfc is the Gaussian error function [17]. Since the channel availability is close to 1, e.g., 99% and μ^* is the small margin for compensating for the prediction error of 1 ~ 2 dB, we can assume $\mu^* \cdot Pr\{\alpha \ge L\}$ is negligible. Thus, we conclude that the power gain G is

$$G \cong \mu \frac{1}{m^2} e^{2\sigma^2} - \mu^*. \tag{3.29}$$

For example, if we try the data measured on a light rain day and shown in Fig. 2.4 (a) with μ = 15 dB and μ^* = 2 dB, we can obtain G = 20 with a sample mean $\hat{m}$ = 1.23 and a sample variance $\hat{\sigma}^2$ = 0.014. Also, for the data on a moderate rain day shown in Fig. 2.4 (b) and the data on a heavy rain day shown in Fig. 2.4 (c), we can have G = 5.15 ($\hat{m}$ = 2.27 and $\hat{\sigma}^2$ = 0.046) and G = 0.42 ($\hat{m}$ = 4.00 and $\hat{\sigma}^2$ = 0.0077) respectively. Since we set the non-adaptive power margin μ for the worst case, i.e., heavy rain, we can obtain better gain in better weather conditions.

However, in Section 2.2 and 2.3 we showed that α can be considered stationary only conditionally according to the weather conditions, i.e., the signal attenuation level, which means that m and σ^2, which characterize a lognormal PDF $p_\alpha(\alpha)$, vary as the weather condition changes with time. Therefore, we need to classify the weather conditions into some states according to the rain rate, such as clear, light rain, moderate rain, and heavy rain state, each of which is represented by its own $p_\alpha(\alpha)$. Then, (3.29) is valid only inside of one weather condition state and the exact total power gain is

$$\overline{G} = \mu \sum_{k = C, L, M, H} \left(\frac{1}{m_k^2} e^{2\sigma_k^2} \right) Pr(k) - \mu^*, \tag{3.30}$$

where C, L, M, and H stand for each weather condition state of clear, light rain, moderate rain, and heavy rain, and $Pr(k)$ is the probability that the weather condition state is k.[1]

With Adaptive Power and Rate Control Together

Here, we consider the adaptive scheme, where both power and rate adaptive control are implemented together.

Fig. 3.12 shows the relation between the received signal energy and signal attenuation for both schemes in this case. E_0 denotes the initial transmitter signal energy to assure the highest rate R_1 of the adaptive scheme at a given target BER. The non-adaptive scheme has the lowest data rate R_N for the same reason as explained in 3.5. 2, and the fixed margin μ of the non-adaptive scheme is chosen to assure this rate even at the largest attenuation L, where the channel turns off. $\mu_i E_0$ denotes the required signal energy to provide the data rate R_i in each modulation/coding state.

1. Crane and the International Radio Consultative Committee, CCIR, have respectively developed rain rate prediction models for global climate regions [10], from which we can obtain the statistics of weather conditions.

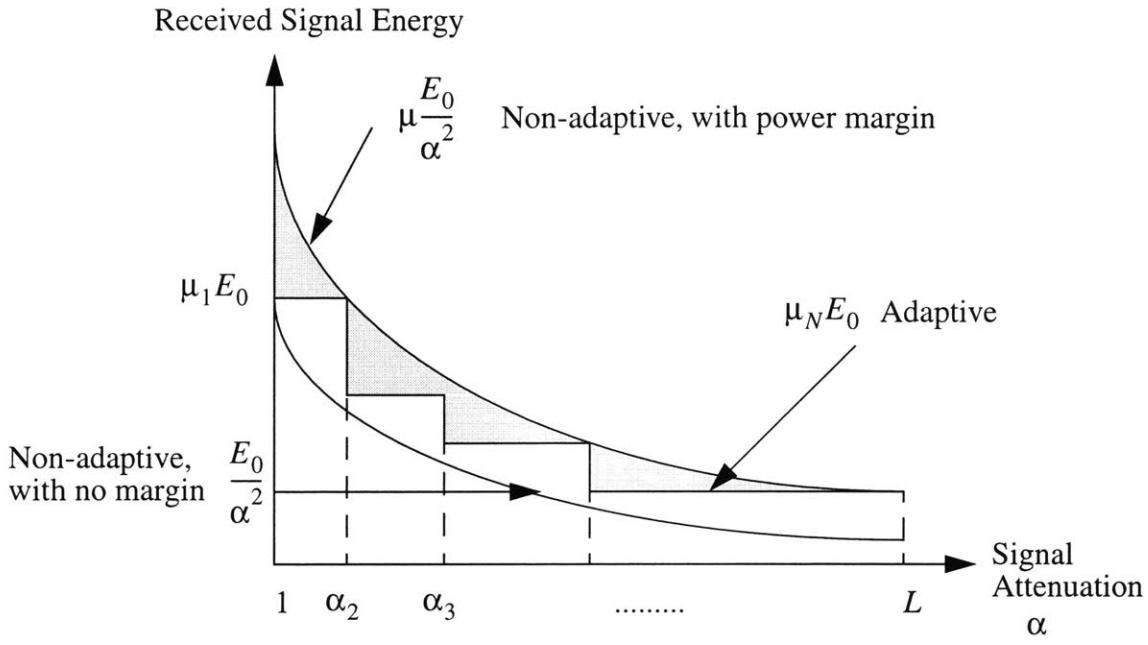

Figure 3.12: Relation between the Received Signal Energy and Signal Attenuation for the Adaptive (with Power and Rate Control Together) and the Non-adaptive Scheme

Then the average power increase of the non-adaptive scheme in this case is the same as in the case of power control only, i.e.,

$$E[\Delta_{non-ad}] = \int_0^L \left(\mu\frac{E_0}{\alpha^2} - \frac{E_0}{\alpha^2}\right) p_\alpha(\alpha)d\alpha. \tag{3.31}$$

The average power increase of the adaptive scheme with both power and rate control together is[1]

1. Though we have defined $\alpha_1 = 1$ previously, we extend State 1 to include $0 < \alpha < 1$ for the same reason as in 2.2.2.

$$E[\Delta_{ad}] = \sum_{i=1}^{N} \int_{\alpha_i}^{\alpha_{i+1}} \left(\mu_i E_0 - \frac{E_0}{\alpha^2} \right) p_\alpha(\alpha) d\alpha$$

$$= \sum_{i=1}^{N} \mu_i E_0 Pr\{state \ \ i\} - \int_0^L \frac{E_0}{\alpha^2} p_\alpha(\alpha) d\alpha$$

$$= \bar{\mu} E_0 - \int_0^L \frac{E_0}{\alpha^2} p_\alpha(\alpha) d\alpha, \tag{3.32}$$

where $\bar{\mu}$ is the mean of μ_i's.

Therefore, with the adaptive power and rate control together, the power gain G represented by the shaded region in Fig. 3.12 is

$$G = \frac{E[\Delta_{non-ad}] - E[\Delta_{ad}]}{E_0}$$

$$= \int_0^L \mu \frac{1}{\alpha^2} p_\alpha(\alpha) d\alpha - \bar{\mu}$$

$$= \int_0^\infty \mu \frac{1}{\alpha^2} p_\alpha(\alpha) d\alpha - \bar{\mu} - \int_L^\infty \mu \frac{1}{\alpha^2} p_\alpha(\alpha) d\alpha$$

$$= \mu \frac{1}{m^2} e^{2\sigma^2} - \bar{\mu} - \int_L^\infty \mu \frac{1}{\alpha^2} p_\alpha(\alpha) d\alpha. \tag{3.33}$$

The last term can be bounded as follows:

$$0 \le \int_L^\infty \mu \frac{1}{\alpha^2} p_\alpha(\alpha) d\alpha \le \frac{\mu}{L^2} \cdot Pr\{\alpha \ge L\}. \tag{3.34}$$

In the same way as in the previous case, with small μ / L^2 and a small probability of outage, we can conclude that

$$G \cong \mu \frac{1}{m^2} e^{2\sigma^2} - \bar{\mu}. \tag{3.35}$$

Also, in this case, we should take into account the fact that α is stationary only conditionally according to weather conditions. Then, the power gain $\bar{G}$ is

$$\bar{G} = \sum_{k = C, L, M, H} \left\{ \mu \left(\frac{1}{m_k^2} e^{2\sigma_k^2} \right) - \bar{\mu}|_k \right\} Pr(k), \tag{3.36}$$

where C, L, M, and H stand for each weather condition state of clear, light rain, moderate rain, and heavy rain, and $Pr(k)$ is the probability that the weather condition state is k.

3.5.4 Upper Bound of Communication Performance

In this subsection, we evaluate the effectiveness of our adaptive power and rate control scheme, and compare the results to some simple upper bounds based on channel capacity arguments. For a simple analysis, we only deal with the adaptive M-PSK case introduced in 3.4.1.

First, we provide a lemma [18].

Lemma:

Let $C(k)$ denote the channel capacity of a discrete memoryless channel (DMC) when M-PSK ($M = 2^k$) modulation is used. Then, $C(k)$ is a nondecreasing function of k.

Proof:

Let us consider a DMC with $2M$ inputs and $2M$ outputs in Fig 3.13, which models a channel using $2M$-PSK modulation, where $M = 2^k$. And we assume that, by a proper choice of input distribution $Q^*_{2M}(x)$, we can achieve the channel capacity $C(k + 1)$.

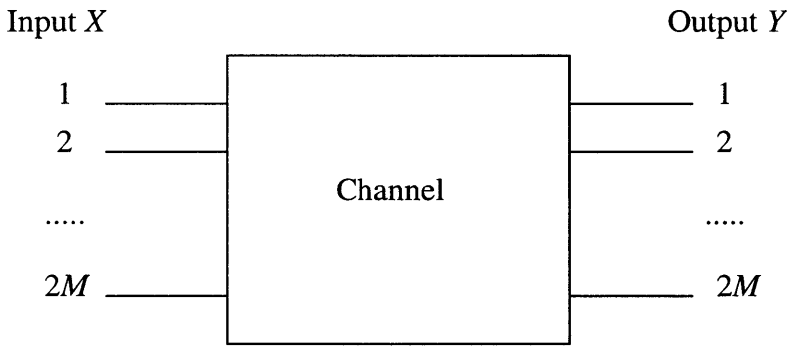

Figure 3.13: $2M$-ary Input-Output Channel

Then, we add suitable input and output processors A and B respectively, through which new M inputs X' are connected to X and new M outputs Y' are connected from Y. In particular, we set the mapping through A as follows:

$$X(i) = X'\left(\frac{i+1}{2}\right) \quad \text{if } i \text{ odd} \tag{3.37}$$

$$0 \qquad \text{if } i \text{ even,}$$

i.e., we simply delete every other (even) inputs from the $2M$-PSK channel.

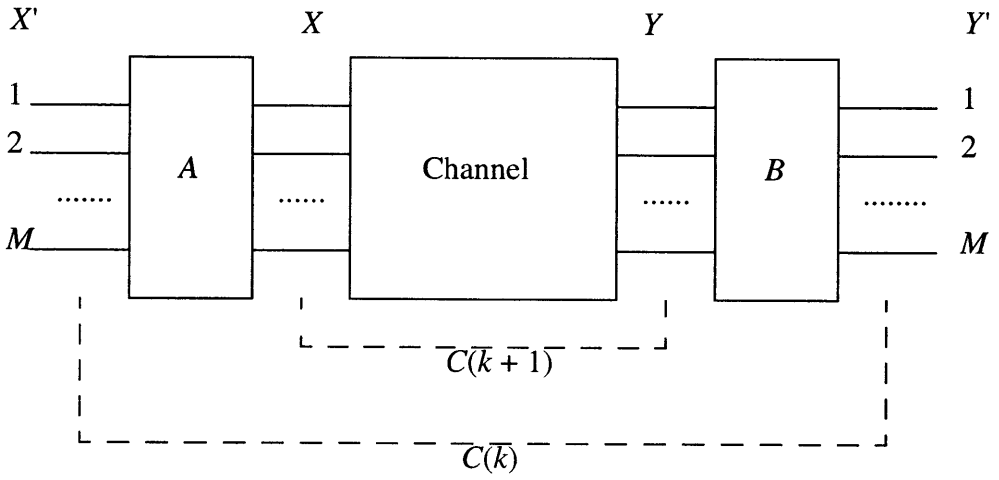

Figure 3.14: M-ary Input-Output Channel

Now, we have a new DMC with M inputs X' and M outputs Y', which consists of a given DMC with $2M$ inputs X, $2M$ outputs Y and processors A and B, and this channel, which is an M-PSK channel, has the capacity $C(k)$ with an input distribution $Q^*_M(x')$. Then with this input distribution, we obtain

$$I(X;Y) = I(X';Y) \geq I(X';Y') = C(k), \tag{3.38}$$

where the first equality follows from the fact that X and X' are identical when we ignore even x terms, the inequality follows from the data processing theorem that if $X \rightarrow Y \rightarrow Z$, then $I(X;Y) \geq I(X;Z)$ [19], and the last equality is from our assumption that $Q^*_M(x')$ achieves $C(k)$. Then, by the definition of $C(k+1)$, $C(k+1) \geq I(X;Y) \geq C(k)$. Therefore, we can conclude that $C(k)$ is a nondecreasing function of k.

This lemma is for the case of hard decision. The case of soft decision can be proved in the same way except that we do not need the output processor B since we do

not have discrete outputs. Of course, since there is no restriction to outputs, soft decision can yield the higher capacity than hard decision. ■

Therefore, with the adaptive symbol size scheme, we can always obtain higher channel capacity than with the one symbol size scheme that uses the smallest symbol size for the requirement on the BER and the availability as we have seen in the previous subsection. The pragmatic and practical question is how quickly $C(k)$ saturates, and gains no longer justify the added complexity. We can calculate the hard decision channel capacity when an M-PSK modulation scheme is used. The channel is modeled as in Fig 3.15.

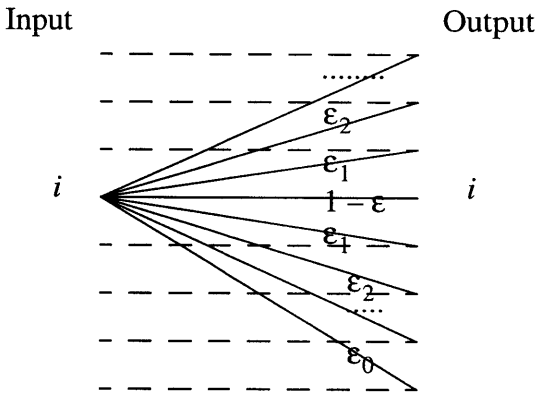

Figure 3.15: Channel with M-PSK Modulation

We assume that the transmission errors occur symmetrically for the two symbols at the same distance with the probability of error ε_i for $i = 1, \ldots, (M-2)/2$, and ε_0 for the symbol in the opposite direction with the distance $2\sqrt{E_s}$. Then, by the symmetry of the

channel, a uniform input distribution $p_X(x) = \frac{1}{M}$, which also results in a uniform output distribution, achieves the channel capacity given by [20]:

$$\begin{aligned} C(k) &= max_{p_X(x)}\ I(X;Y) \\ &= max_{p_X(x)} \sum_x \sum_y p_{X,Y}(x,y) \log \frac{p_{X,Y}(x,y)}{p_X(x)p_Y(y)} \\ &= \sum_x \sum_y p_{Y|X}(y|x) \frac{1}{M} \log \frac{p_{Y|X}(y|x)}{1/M} \\ &= \sum_x \sum_y p_{Y|X}(y|x) \frac{1}{M} \log M + \sum_x \sum_y \frac{1}{M} p_{Y|X}(y|x) \log p_{Y|X}(y|x) \\ &= \log M + 2 \sum_{i=1}^{(M-2)/2} \varepsilon_i \log \varepsilon_i + \varepsilon_0 \log \varepsilon_0 + (1-\varepsilon)\log(1-\varepsilon), \end{aligned} \tag{3.39}$$

where $\varepsilon \equiv \varepsilon_0 + 2 \sum_{i=1}^{(M-2)/2} \varepsilon_i$ and $M = 2^k$. For good symbol error probabilities, we can ignore all ε_i's except ε_1, which is for the nearest neighbor signals. In this case, we can get

$$C(k) \cong \log M + 2\varepsilon_1 \log \varepsilon_1 + (1-2\varepsilon_1)\log(1-2\varepsilon_1), \tag{3.40}$$

and ε_1 is given as in 3.4.1 as follows:

$$\varepsilon_1 \cong 2Q\left(\sqrt{2\frac{E_s}{N_0}} \sin\left(\frac{\pi}{M}\right)\right). \tag{3.41}$$

By the lemma, this capacity increases as M increases. However, we know that the band-limited Gaussian channel can achieve the maximum channel capacity [19]:

$$C = W \log\left(1 + \frac{P}{N_0 W}\right), \qquad \text{bits per second} \tag{3.42}$$

where W is the bandwidth of the channel, $N_0/2$ is the power spectral density of AWGN, and P is the signal power. If a symbol duration is assumed to be T, the capacity is

$$C = WT\log\left(1 + \frac{E_s}{N_0 WT}\right), \qquad \text{bits per transmission} \tag{3.43}$$

where $E_s = PT$ is the signal energy per symbol, and for the two dimensional case, we have $2WT = 2$, i.e., $WT = 1$. This is an upper bound for $C(k)$ with the same SNR, which is shown in Fig. 3.16. $C(k)$ is also a factor of 2 away from the Shannon capacity limit because the modulation scheme is not optimal, but used mostly because of simplicity and hardware constraints. QAM, for example, is most efficient but much harder to implement in a satellite channel.

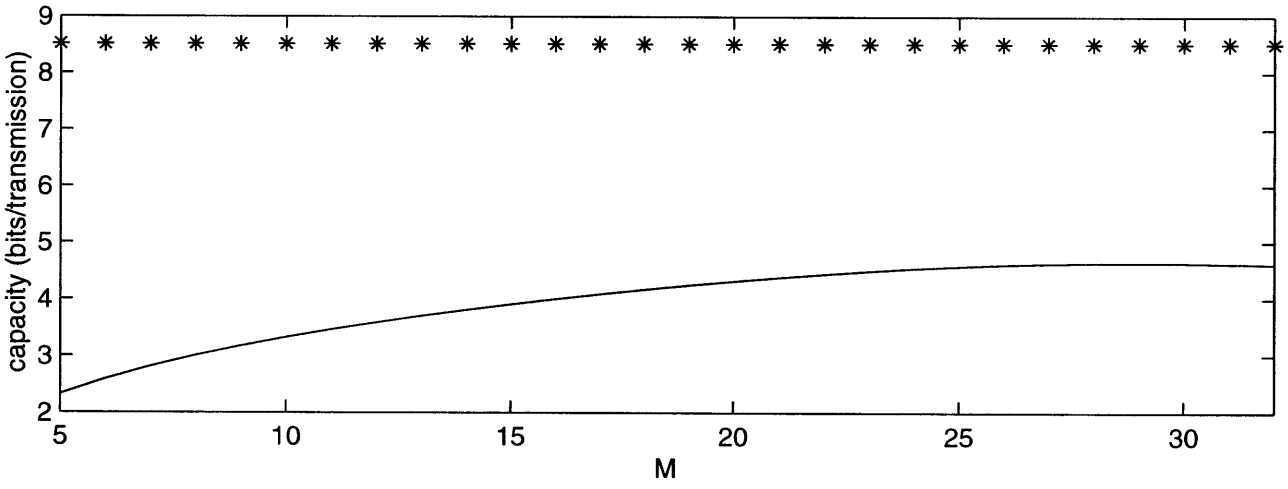

Figure 3.16: Capacity of the Channel with M-PSK Modulation (solid) vs. Capacity of the Band-limited Gaussian Channel (stars) along Symbol Size M ($E_s/N_0 = 25$ dB)

Fig 3.17 shows that our adaptive scheme can use data rates R_i's with an appropriate choice of coding below the $C(i)$'s, yielding the average rate:

$$\bar{R} = \sum_{i=1}^{N} R_i \int_{\alpha_i}^{\alpha_{i+1}} p_\alpha(\alpha) d\alpha, \tag{3.44}$$

while the non-adaptive scheme has the fixed lowest capacity of BPSK with the same target BER and availability. As we have seen in 3.4.1, the state boundaries are selected to secure the BER below a given target BER at a given availability.

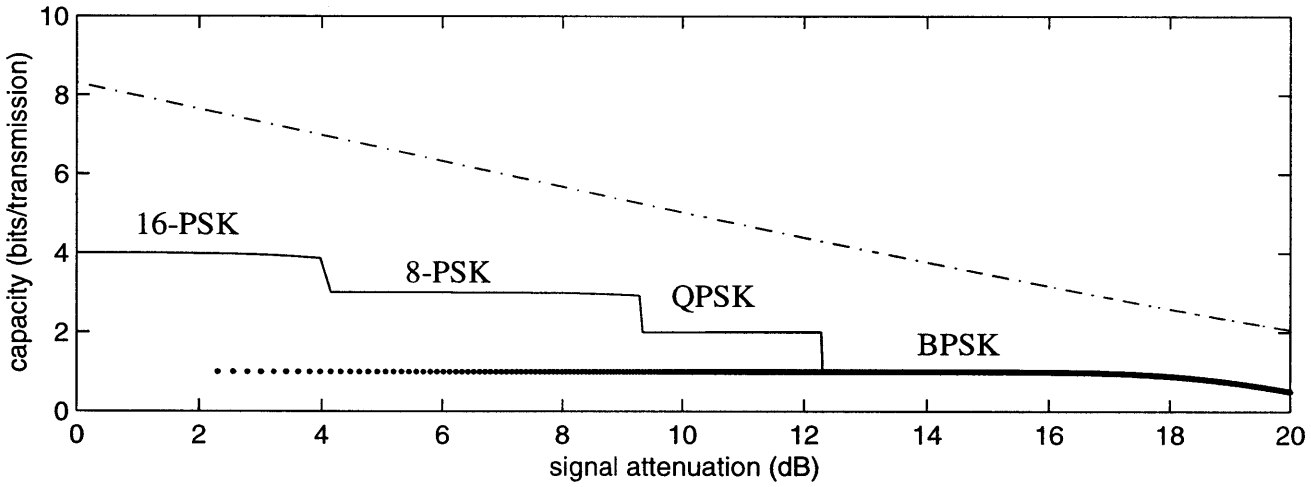

Figure 3.17: Capacity of the Channel with *M*-PSK Modulation (solid) vs. Capacity of the Band-limited Gaussian Channel (dotted) along Signal Attenuation, also Compared with a Fixed Capacity of the Non-adaptive Scheme (points)

3.6 Summary

This chapter presented channel adaptation methods based on the channel models and the prediction techniques developed in Chapter 2.

We considered changing the signal transmission power, the modulation symbol size, and the code rate adaptively for channel adaptation, and in particular, suggested a continuous power control and discrete rate control scheme. We built a set of modulation/coding states, each of which has a fixed rate, and discretely changed the modulation symbol size and/or the code rate correspondingly from state to state. Within a state, continuous power control was implemented, so that we moved the operation point to the optimal point, the lower signal attenuation boundary of the state. Through this strategy, we could adapt the data rate to yield the target BER at a given availability, consuming the most efficient amount of power.

Then, we illustrated how to set the signal attenuation boundaries of the data rate states using various modulation/coding schemes such as *M*-PSK, *M*-QAM, punctured convolutional codes, and trellis coded modulation.

Finally, we gave the performance analysis in consideration of such parameters as the availability, the average rate, and the average power increase. Our analysis showed that with the adaptive scheme there is substantial improvement in required power and capacity for the same availability compared to the non-adaptive scheme. With adaptive power control only, we could obtain the power gain of

$$G \cong \mu \frac{1}{m^2} e^{2\sigma^2} - \mu^*, \tag{3.45}$$

where $\ln m$ and σ^2 are the mean and the variance of $\ln\alpha$ respectively, μ is the fixed

power margin in the non-adaptive scheme, μ^* is the fixed small power margin provided to compensate for the prediction error in the adaptive scheme, and E_0 is the initial transmitter signal energy per symbol to yield a given data rate below a given target BER. We showed that we can get $G = 20$, 5.15, and 0.42 on a light rain day, a moderate rain day, and a heavy rain day respectively, with some sample data. However, since α is stationary only conditionally according to weather conditions, we needed to classify the weather conditions according to rain rate, and consider the different statistics of α within each weather condition and geographical region, which resulted in the power gain of

$$\overline{G} \cong \mu \sum_{k = C, L, M, H} \left(\frac{1}{m_k^2} e^{2\sigma_k^2} \right) Pr(k) - \mu^*, \tag{3.46}$$

where C, L, M, and H stand for each weather condition state, and $Pr(k)$ is the probability that the weather condition state is k (geographical-region-specific, from experimental characterization). With adaptive power and rate control together, the power gain was

$$\overline{G} \cong \sum_{k = C, L, M, H} \left\{ \mu \left(\frac{1}{m_k^2} e^{2\sigma_k^2} \right) - \bar{\mu}|_k \right\} Pr(k), \tag{3.47}$$

where μ is the fixed margin of the non-adaptive scheme, $\bar{\mu}$ is the mean of the required power margin μ_i in each modulation/coding state i, and E_0 is the initial transmitter signal energy to assure the highest rate of the adaptive scheme with the given target BER.

The analysis of the upper bound of the data rate with the adaptive M-PSK scheme showed that the channel capacity is a nondecreasing function of M, and upper-bounded by the capacity of the Gaussian channel. Then, we have compared the capacity of the adaptive symbol size scheme to that of the one symbol size scheme. In practice, one can obtain adaptive data rates with some practical coding schemes below the channel capacity, yielding the average rate,

$$\bar{R} = \sum_{i=1}^{N} R_i \int_{\alpha_i}^{\alpha_{i+1}} p_{\alpha}(\alpha) d\alpha, \tag{3.48}$$

while the non-adaptive scheme has the fixed lowest rate R_N with the same target BER and availability.

Chapter 4

Conclusions and Future Research

4.1 Conclusions

In this thesis, we have characterized satellite channels at high frequencies (above 10 GHz) with weather-induced impairments, and developed channel prediction and adaptation methods over these channels.

We considered scintillation and rain attenuation as two dominant causes of the signal fading process over satellite-earth channels at high frequencies, e.g., Ka-band. Two processes of scintillation and rain attenuation have been modeled as random processes for short durations with lognormally distributed PDFs, which are conditionally stationary according to weather conditions. Statistical and spectral analyses of the attenuated signals using AR modeling have been then discussed. The rain attenuation process had a PSD with a slope of -20 dB/decade (f^{-2}) and a corner frequency of the order of 10^{-3} ~ 10^{-4} Hz. For scintillation, a slope ranged -23 ~ -37 dB/decade ($f^{-2.3} \sim f^{-3.7}$) and a corner frequency was of the order of 0.1 Hz. With this information, we could obtain the 1st or 2nd order of autoregressive LLS (moreover, MMSE in Gaussian environments) estimators for future signal attenuation. Using these estimators, it was possible to predict the received

signal attenuation within ±0.5 dB 1 second ahead and within ±1.0 dB 4 seconds ahead in the examples of Section 2.4.

Then, for channel adaptation, we have investigated the possibilities for performance improvement by adaptively changing the signal transmission power, the modulation symbol size, and the code rate according to the predicted future signal attenuation. The scheme that has been suggested for channel adaptation and discussed in detail throughout Chapter 3 was a continuous power control and discrete rate control scheme. Along the received signal attenuation levels we set a finite number of modulation/coding states, each of which had a fixed data rate with a specific modulation/coding scheme, and discretely changed the corresponding modulation/coding when the predicted future signal attenuation crossed over the boundary of the state. Within a state, we have implemented continuous power control, through which the constant SNR that is required for a target BER at a given availability has been maintained, so that we could keep the operation point at the optimal point inside the state. In the examples of Section 3.4, we have also shown that we could set the state boundaries with such modulation/coding schemes as M-PSK, M-QAM, punctured convolutional codes, and trellis coded modulation. Our analyses indicated that there could be substantial performance improvement on capacity and power consumption using the adaptive control schemes.

4.2 Future Research

One possibility for future research is to develop solid algorithms for channel adaptation with powerful coding schemes, which will be applied to satellite-earth channels in practi-

cal implementations. For candidates of powerful coding, it is known that turbo-codes and low-density parity-check (LDPC) codes closely approach Shannon's channel capacity limit.

An example of a standard turbo-code [16] is based on a simple 16-state rate-1/2 convolutional encoder in systematic form. The information bits are encoded in the usual way in this encoder to generate a first check sequence; they are then scrambled in a long interleaver, and encoded again to generate a second check sequence. The information bits and the two check sequences are all transmitted, yielding a rate-1/3 code. At the receiver, the information sequence and the first check sequence are decoded by a "soft-in, soft-out" decoding algorithm that produces reliability metrics for each decoded information bit. These reliability metrics are then used in a "soft decoding" of the second code (using the same information sequence, in a permuted order) to produce improved estimates of the reliabilities of the information bits, which can then be used by the first decoder. This process may be iterated for 10 ~ 20 cycles. Amazingly good performance is obtained, within tenths of a dB of the Shannon limit. Furthermore, the association of a turbo-code with a bandwidth efficient modulation (BEM) such as QAM provides additional coding gain [21].

Low-density parity-check codes [16] can outperform turbo-codes. LDPC codes are very long binary linear block codes such that each information bit appears in only a small number of parity checks, and each parity check checks only a small number of information bits. Again, an iterative decoding method may be used to get close to the Shannon limit (within 0.1 dB, with million-bit blocks).

In addition to adaptive forward error control (FEC), automatic repeat request (ARQ) error control may be used to guard against the deepest fades over satellite-terrestrial links resulting in burst errors in received data. A combination of FEC and ARQ systems, so

called a hybrid FEC/ARQ [22], provides the advantages of both techniques. The inner FEC system corrects many channel errors and reduces the requests for retransmissions, while the outer ARQ system provides a very low probability of undetected errors. Therefore, the design of an appropriate hybrid scheme is to handle the trade-off between sufficient throughput and good error performance. Usually, real-time data communications such as video or audio cannot tolerate much delay, hence they prefer the use of FEC. On the contrary, non-real-time data communications such as file transfer require excellent system error performance rather than small delay, which results in the preference of the use of ARQ.

Finally, our technologies of channel modeling, prediction, and adaptation can be coupled with dynamic routing and congestion algorithms in satellite-terrestrial heterogeneous network development. A statistical model of the Physical Layer channel (in terms of stochastically time varying capacity and availability) can be developed as inputs to the tasks in network routing and Transport Layer Protocol development.

Appendix A

Autoregressive (AR) Modeling

Autoregressive (AR) modeling [23], or all-pole filter modeling is a parametric signal modeling method for spectral estimation. In AR modeling, we assume that the power spectral density (PSD) of a process of our interest, $S(z) = H(z)H(1/z)$, is rational and $H(z)$ is autoregressive:

$$H(z) = \frac{A}{1 - \sum_{k=1}^{M} a_k z^{-k}}. \tag{A.1}$$

Let $y[n]$ be a stochastic process that we want to model using the AR modeling method. Then, $y[n]$ is modeled as the output $\hat{y}[n]$ of an all-pole filter $H(z)$ driven by a zero-mean white noise process $w[n]$, and the process $\hat{y}[n]$ satisfies the equation

$$\hat{y}[n] = \sum_{k=1}^{M} a_k \hat{y}[n-k] + Aw[n]. \tag{A.2}$$

Fig. A.1 shows this filtering procedure.

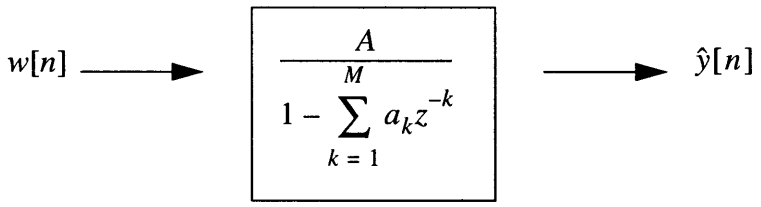

Figure A.1: All-Pole Filter

Since $\hat{y}[n]$ is the estimation of $y[n]$, we wish to choose a_k's to minimize $E[(y[n]-\hat{y}[n])^2]$. However, this approach requires the solutions of a set of nonlinear equations. Therefore, to obtain the linear equations, we follow the inverse approach, where $y[n]$ drives the inverse filter of $H(z)$, so as to yield $g[n]$, the approximation of a white noise process $w[n]$. $1/H(z)$ is called a whitening filter in this case. Fig A.2 shows this inverse filtering procedure.

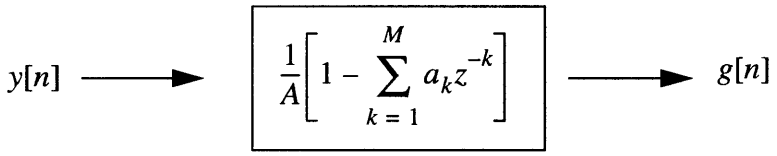

Figure A.2: Inverse of All-Pole Filter

We denote the prediction error $e[n] = g[n]-w[n]$ and want to choose a_k's to minimize

$$\mathcal{E} = E[e^2[n]] = E\left[\left\{\frac{1}{A}\left(y[n]-\sum_{k=1}^{M} a_k y[n-k]\right)-w[n]\right\}^2\right]. \tag{A.3}$$

To determine a_k for $k = 1, 2, ..., M$,

$$\frac{\partial \mathcal{E}}{\partial a_i} = 0 = E\left[-\frac{2}{A}\left\{\frac{1}{A}\left(y[n] - \sum_{k=1}^{M} a_k y[n-k]\right) - w[n]\right\} y[n-i]\right]. \qquad \text{(A.4)}$$

$$\text{for } i = 1, \ldots, M$$

This can be written as follows:

$$E[y[n]y[n-i]] - \sum_{k=1}^{M} a_k E[y[n-k]y[n-i]] - AE[w[n]y[n-i]] = 0. \qquad \text{(A.5)}$$

$$\text{for } i = 1, \ldots, M$$

Since we assume that a zero-mean white noise process $w[n]$ is uncorrelated with $y[n]$, the last term in (A.5) becomes zero. Using the covariance function

$$K_{yy}[m] = E[y[n]y[n+m]], \qquad \text{(A.6)}$$

we can get

$$\sum_{k=1}^{M} a_k K_{yy}[i-k] = K_{yy}[i], \qquad \text{for } i = 1, \ldots, M \qquad \text{(A.7)}$$

which is equivalent to

$$\underbrace{\begin{bmatrix} K_{yy}[0] & K_{yy}[1] & \ldots & K_{yy}[M-1] \\ K_{yy}[1] & K_{yy}[0] & \ldots & \\ \ldots & & & \\ K_{yy}[M-1] & & \ldots & K_{yy}[0] \end{bmatrix}}_{T_M} \underbrace{\begin{bmatrix} a_1 \\ a_2 \\ \ldots \\ a_M \end{bmatrix}}_{\alpha_M} = \underbrace{\begin{bmatrix} K_{yy}[1] \\ K_{yy}[2] \\ \ldots \\ K_{yy}[M] \end{bmatrix}}_{r_M}. \qquad \text{(A.8)}$$

And this can be written as follows:

$$T_M \alpha_M = r_M. \qquad \text{(A.9)}$$

These equations are called *Yule-Walker* equations. A in (A.1) is determined so that the variance (in this case, equivalent to the spectral power) of $w[n]$ and $g[n]$ is equal.

To solve (A.9), it suffices to find a_k's, and thus, we can obtain the AR model of a random process $y[n]$ and its power spectral density $S(z)$. Since the matrix T_M is Toeplitz, i.e., it is symmetrical with respect to its diagonal, (A.9) can be simply solved using this property (e.g., Levinson recursion [23, 24]).

Appendix B

Linear Least-Squares (LLS) Estimation

We know that the minimum mean-square error (MMSE) estimator is optimal. However, this estimator is, in general, a nonlinear function of the data, and computing this estimator requires that we know the complete statistical characterization of the relationship between the observed data and the estimated data. Therefore, we often need to look for suboptimal estimators, one of which is a linear least-squares (LLS) estimator [9]. This estimator, $\hat{x}_{LLS}(\ )$, is defined as

$$\hat{x}_{LLS}(\ ) = \arg min_{\hat{x}_L \in \mathcal{B}} E[\|x - \hat{x}_L\|^2], \tag{B.1}$$

where

$$\mathcal{B} = (\hat{x}_L | \hat{x}_L(y) = Ay + d \text{ for some } A \text{ and } d\} \tag{B.2}$$

and we want to estimate x based on the observations of y.

Following are some properties of LLS estimators.

1. The LLS estimator is always unbiased, i.e.,

$$E[\hat{x}_{LLS}] = E[x]. \tag{B.3}$$

2. (*Orthogonality Principle*)

A linear estimator $\hat{x}_L$ is the LLS estimator, i.e., $\hat{x}_L = \hat{x}_{LLS}$, if and only if the estimation error $e(x, y) = \hat{x}_L(y) - x$ is orthogonal to any vector-valued linear function of the data, i.e.,

$$E[[\hat{x}_L(y) - x][Fy + g]^T] = 0 \tag{B.4}$$

for any constant matrix and vector F and g respectively.

3. If x and y are jointly Gaussian random vectors, then $\hat{x}_{MMSE}(y) = \hat{x}_{LLS}(y)$.

Proof:

Let $e = \hat{x}_{LLS}(y) - x$ and by the orthogonality principle, e is orthogonal to y, which means that e and y are uncorrelated. Since x and y, and eventually e and y are jointly Gaussian, e is independent of y. Thus,

$$E[e|y] = E[e] = 0. \tag{B.5}$$

But we also have

$$\begin{aligned} E[e|y] &= E[\hat{x}_{LLS}(y)|y] - E[x|y] \\ &= \hat{x}_{LLS}(y) - \hat{x}_{MMSE}(y), \end{aligned} \tag{B.6}$$

where the last equality comes from the fact that, given y, the mean of $\hat{x}_{LLS}(y)$ is equal to $\hat{x}_{LLS}(y)$ itself, and the definition of $\hat{x}_{MMSE}(y) = E[x|y]$.

Therefore, $\hat{x}_{LLS}(y) = \hat{x}_{MMSE}(y)$.

References

[1] C. E. Mayer, B. E. Jaeger, R. K. Crane, and X. Wang, "Ka-band Scintillations: Measurements and Model Predictions," *Proc. of IEEE*, vol. 85, no. 6, pp. 936-945, June 1997.

[2] M.- S. Alouini, S. A. Borgsmiller, and P. G. Steffes, "Channel Characterization and Modeling for Ka-Band VSAT," *Proc. of IEEE*, vol. 85, no. 6, pp. 981-997, June 1997.

[3] T. J. Moulsley and E. Vilar, "Experimental and Theoretical Statistics of Microwave Amplitude Scintillations on Satellite Down-Links," *IEEE Trans. on Antennas and Propagation*, vol. AP-30, no. 6, pp. 1099-1106, November 1982.

[4] V. W. S. Chan, private communication, December 1999.

[5] J. E. Allnutt, *Satellite-to-ground Radiowave Propagation*, Peter Peregrinus Ltd., 1989.

[6] T. Maseng and P. M. Bakken, "A Stochastic Dynamic Model of Rain Attenuation," *IEEE Trans. on Comm.*, vol. COM-29, no. 5, pp. 660-669, May 1981.

[7] A. Burgueno, E. Villar, and M. Puigcerver, "Spectral Analysis of 49 Years of Rainfall Rate and Relation to Fade Dynamics," *IEEE Trans. on Comm.*, vol. 38, no. 9, pp. 1359-1366, September 1990.

[8] E. Matricciani, "Physical-mathematical Model of Dynamics of Rain Attenuation with Application to Power Spectrum," *Electronics Letters*, vol. 30, no. 6, pp. 522-524, 17th March 1994.

[9] A. S. Willsky, G. W. Wornell, and J. H. Shapiro, *6.432 'Stochastic Processes, Detection, and Estimation' Course Notes,* MIT EECS, 1999.

[10] L. J. Ippolito Jr., *Radiowave Propagation in Satellite Communications*, New York: Van Nostrand Reinhold Company, 1986.

[11] S. G. Wilson, *Digital Modulation and Coding*, Upper Saddle River: Prentice Hall, 1996.

[12] R. A. Nelson, "The Art of Communication via Satellite," *Satellite Today*, Phillips Publishing International, July 1998.

[13] S. Haykin, *Communication Systems*, 3rd ed., New York: John Wiley & Sons, 1994.

[14] D. Haccoun and G. Begin, "High-Rate Punctured Convolutional Codes for Viterbi and Sequential Decoding," *IEEE Trans. on Comm.*, vol. 37, no. 11, pp. 1113-1125, November 1989.

[15] Y. Yasuda, K. Kashiki, and Y. Hirata, "High-Rate Punctured Convolutional Codes for Soft Decision Viterbi Decoding," *IEEE Trans. on Comm.*, vol-COM. 32, no. 3, pp. 315-319, March 1984.

[16] G. D. Forney Jr., *6.451 'Principles of Digital Communication' Course Notes*, MIT EECS, 1999.

[17] V. W. S. Chan, "Coding for the Turbulent Atmospheric Optical Channel," *IEEE National Telecommunications Conference*, November 1979.

[18] V. W. S. Chan, private communication, April 2000.

[19] T. M. Cover and J. A. Thomas, *Elements of Information Theory*, John Wiley & Sons, 1991.

[20] R. G. Gallager, *Information Theory and Reliable Communication*, John Wiley & Sons, 1968.

[21] S. Le Goff, A. Glavieux, and C. Berrou, "Turbo-Codes and High Spectral Efficiency Modulation," *Proc. ICC* '94 (New Orleans, LA), pp. 645-649, May 1994.

[22] V. K. Bhargava, D. Haccoun, R. Matyas, P. P. Nuspl, *Digital Communications by Satellite*, John Wiley & Sons, 1981.

[23] A. V. Oppenheim, *6.341 'Discrete-Time Signal Processing' Lecture Notes*, MIT EECS, 1999.

[24] A. Papoulis, *Probability, Random Variables, and Stochastic Processes*, 3rd ed, McGraw-Hill, 1991.